

Collective spin excitations of helices and magnetic skyrmions: review and perspectives of magnonics in non-centrosymmetric magnets

Markus Garst¹, Johannes Waizner² and Dirk Grundler³

¹ Institut für Theoretische Physik, TU Dresden, 01062 Dresden, Germany

² Institut für Theoretische Physik, Universität zu Köln, Zùlpicher Str. 77a, 50937 Köln, Germany

³ Institute of Materials (IMX) and Institute of Microengineering (IMT), Laboratory of Nanoscale Magnetic Materials and Magnonics, School of Engineering, École Polytechnique Fédérale de Lausanne (EPFL), 1015 Lausanne, Switzerland

E-mail: markus.garst@tu-dresden.de, dirk.grundler@epfl.ch

January 2017

Abstract. Magnetic materials hosting correlated electrons play an important role for information technology and signal processing. The currently used ferro-, ferri- and antiferromagnetic materials provide microscopic moments (spins) that are mainly collinear. Recently more complex spin structures such as spin helices and cycloids have regained a lot of interest. The interest has been initiated by the discovery of the skyrmion lattice phase in non-centrosymmetric helical magnets. In this review we address how spin helices and skyrmion lattices enrich the microwave characteristics of magnetic materials and give rise to bottom-up magnonic crystals. When discussing perspectives for microwave electronics and magnonics we focus particularly on insulating materials as they avoid eddy current losses, offer low spin-wave damping, and allow for electric field control. Thereby, they further fuel the vision of magnonics operated at low energy consumption.

1. Introduction: magnets for high-frequency applications

Ferromagnetic materials played a dominant role in non-volatile data storage for decades. They dominated the perception of technology-relevant magnetic[‡] materials. In ferromagnets, microscopic magnetic moments (spins) align in parallel [Fig. 1 (a)] and lead to both a large static susceptibility χ and a large saturation magnetization M_s that allows one to encode data.

The functionality and relevance of antiferromagnets are often less appreciated as their spins are antiparallel [Fig. 1 (b)] and can completely compensate each other: M_s becomes zero for perfect magnetic order. In fact, when discussing antiferromagnets in his Nobel prize lecture Louis Néel argued in 1970 that antiferromagnetic materials were extremely interesting from the theoretical viewpoint, but did not seem to have any application [2]. This viewpoint drastically changed after modern sensing applications

[‡] Note that we address materials that show cooperative magnetic phenomena such as ferromagnetism, ferrimagnetism and antiferromagnetism. We do not consider diamagnetism and paramagnetism.

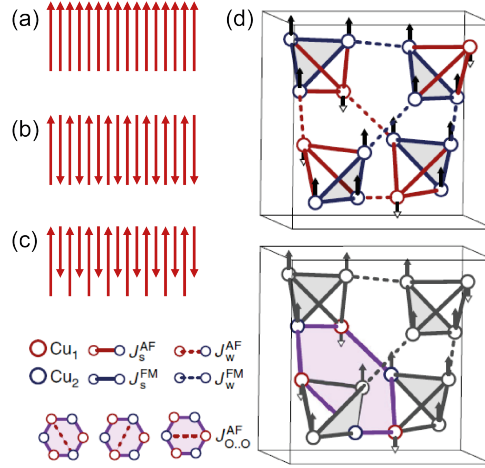


Figure 1. Spins configuration representing (a) ferromagnetic, (b) antiferromagnetic and (c) ferrimagnetic order assuming two sublattices of different spin moments. (d) Orientation of magnetic moments attributed to Cu ion sublattices in the chiral magnetic insulator Cu_2OSeO_3 . Connecting lines categorize different exchange interactions: (top) first-neighbour ferromagnetic (FM) (blue) and antiferromagnetic (AF) (red) couplings. Strong (weak) bonds are indicated with solid (dashed) lines. Bottom: Further neighbour antiferromagnetic interaction realized on the diagonals of hexagons formed by alternating Cu_1 and Cu_2 sites. Compare legend on the left. Figure Symmetrized TOF data along high-symmetry directions rearranged from Ref. [1] published under CC-BY.

and information technology required smaller and smaller ferromagnetic devices. In the course of miniaturization, they faced reduced stability due to environmental influences such as stray fields and increased operational temperatures. Nowadays the compensating spin structure of antiferromagnets plays an important role for stabilizing ferromagnets via exchange bias [3].

In Ref. [2] Louis Néel discussed also the more complex spin structures of ferrites and ferrimagnets [Fig. 1 (c)] where sublattices of collinear spins but different $M_{s,i}$ (numbered with $i = 1, 2$) couple antiferromagnetically. The ferrites were technologically relevant since the 1930's. They are still produced in large amounts of several 100 000 t per year. Ferrimagnetic garnets are also of particular interest for applications. Following Ref. [2] they are excellent insulators, can be prepared in large crystals, and can be used at very high frequencies in a large number of devices as their magnetization dynamics exhibits very sharp resonance lines. Accordingly, the insulating ferrimagnet yttrium iron garnet $\text{Y}_3\text{Fe}_5\text{O}_{12}$ (YIG) is exploited in microwave technologies such as circulators, band-pass filters and oscillators, ranging from radar applications to vector network analyzers [4, 5]. The relevant frequency regime ranges roughly from 0.5 to 50 GHz. Bulk YIG exhibits an extremely sharp resonance line and the smallest damping parameter α ever measured for magnetic resonances in ferro-, ferri- or antiferromagnetic materials. At room temperature its record value amounts to about $\alpha = 3 \times 10^{-5}$ [6, 7]. Metals have not yet reached this low level of damping [8]. Consequently, YIG has taken a key role in the research field of *magnonics* [9, 10, 11] where one aims at information processing using collective spin excitations in the form of spin waves (magnons) [9, 12, 13, 14, 15]. Spin waves as information carriers

transport angular momentum but no charges. Thereby spin-wave based interconnects on chips [16], spin-wave logic [17, 18] and on-chip microwave electronics avoid Joule heating and, in general, offer operation at low power consumption. Electric-field control of spin waves would offer even further reduced power consumption.

The advantages of magnonics can be harvested if one exploits spin-wave wavelengths smaller than 100 nm [14]. Recently, nanopatterned magnetic materials with periodically modulated properties have provided a promising avenue in that magnonic grating couplers excited spin waves with wavelengths as small as 68 nm based on conventional microwave components operated at a few GHz [11]. The wavelength of spin waves was smaller by a factor of about 300 000 compared to the corresponding electromagnetic wave in free space. This enormous wavelength reduction is a further key aspect of magnonics. The relevant magnonic grating couplers were realized by integrating periodic arrays of metallic ferromagnetic nanodisks to a thin YIG film [11]. Even earlier it was shown that bicomponent periodic lattices formed magnonic crystals (MCs) providing artificially tailored spin-wave band structures consisting of allowed minibands and forbidden frequency gaps [19, 20]. A periodic lattice of nanostripes [19] or nanodisks [20] introduced a periodic potential which induced Bragg scattering of spin waves [21]. Strikingly, periodically patterned ferromagnetic materials allow one to create magnonic crystals with reconfigurable wave properties. Via different magnetic states one-and-the-same magnonic crystal can exhibit different forbidden frequency gaps and Brillouin zone boundaries (for a review see Ref. [22]). To control the band structure for spin waves on demand different techniques have been explored or suggested such as e.g. magnetic fields [23, 24, 25], current pulses [26], light patterns [27], thermally assisted scanning probe lithography [28] and electric fields [29]. Periodically arranged domain walls have been suggested as a further interesting building block for MCs. Here, non-collinear spin structures if realized in a plain film would avoid nanopatterning and allow for MCs with reconfigurable properties as well [30]. The same holds true for periodic arrays of bubble domains in garnets [31].

Interestingly, chiral magnetic materials possess magnetic properties that are *intrinsically* periodic (Fig. 2). Periods (lattice constants) are on the nanoscale (compare parameter $2\pi/Q$ in Tab. 1) and, hence, extremely interesting for nanomagnonics. In chiral magnets, non-collinear spin structures are stabilized by the Dzyaloshinsky-Moriya interaction (DMI) attributed to relativistic spin-orbit coupling [32]. Examples are materials such as the metals MnSi, FeGe, the semiconductor $\text{Fe}_{0.8}\text{Co}_{0.2}\text{Si}$ and the insulator Cu_2OSeO_3 [33] that all possess a non-centrosymmetric cubic crystal structure with space group $P2_13$ (Tab. 1). They share the same magnetic phases that include periodic helical and conical spin structures as well as a skyrmion phase, see Fig. 2 and the review of Ref. [47]. Skyrmions are particle-like spin textures (spin solitons) that exhibit nanometer-sized dimensions and a long lifetime due to topological protection [48, 49]. They were first discovered in the magnetic phase diagram of the metallic chiral magnet MnSi [50, 51]. In bulk materials, they form a periodic magnetic skyrmion lattice (SkL) [Fig. 2 (e)] with hexagonal symmetry, sometimes also called skyrmion crystal [52].

Individual skyrmions are already foreseen to advance spintronics [53] and to provide a new platform for the race track memory [54, 55, 56], for magneto-logic [57] and GHz oscillators [58, 59, 60]. The term *skyrmionics* summarizes the research efforts that aim at skyrmion-based electronics. Here ultrathin metallic layers exhibiting spin-orbit coupling and interfacial DMI are currently preferred [61, 62, 63]. On the one hand, based on such layers, skyrmions have been stabilized at room temperature

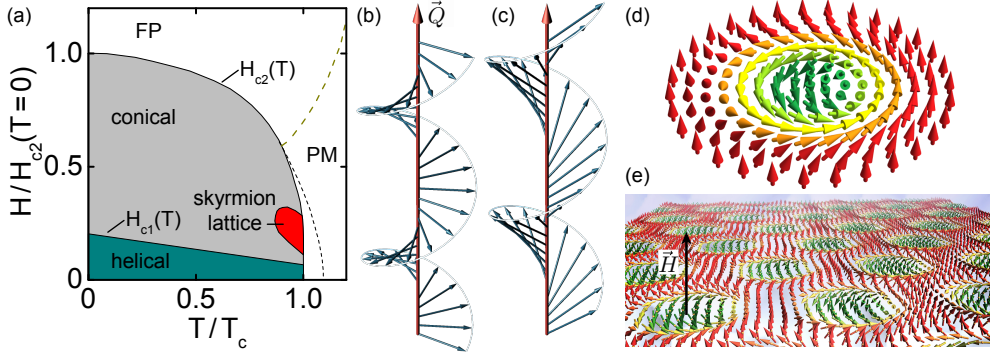


Figure 2. (a) Qualitative magnetic phase diagram of the cubic chiral helimagnets defining the critical field H_{c2} and the critical temperature T_c (PM: paramagnetic, FP: field polarized state). Illustrations of (b) helical and (c) conical spin texture. Q is the helical propagation vector. (d) Spin texture of an individual magnetic skyrmion (Bloch-type). (e) Skyrmion lattice forming in a plane perpendicular to the applied field H .

Table 1. Overview and parameters of selected skyrmion-hosting materials.

Material	Space group	Type	$\frac{2\pi}{Q}$ [nm]	T_c [K]	$\chi_{\text{con}}^{\text{int}}$	$\frac{\omega_{c2}^{\text{int}}}{2\pi}$ [GHz]	magnetic resonances	inelastic neutron scattering
MnSi ^a	P2 ₁ 3	metal	18	29	0.34	16.7	[34, 35]	[36, 37]
Cu ₂ OSeO ₃ ^a	P2 ₁ 3	insulator	60	58	1.76	2.3	[34, 38, 39]	[1, 40]
Fe _{0.8} Co _{0.2} Si ^a	P2 ₁ 3	semicond.	34	28	0.65	4.4	[34, 41]	
FeGe ^a	P2 ₁ 3	metal	70	278	3.43		[42, 43] ^c	[44]
GaV ₄ S ₈ ^b	R3m	semicond.	22	11			[45, 46]	

^ahelical and Bloch-type skyrmions; ^bcycloidal and Néel-type skyrmions; ^cGHz resonances were measured on FeGe that was deposited as a thin film on a substrate

[64, 65, 66, 67]. On the other hand, the multilayers allow for the exploitation of existing thin-film deposition techniques and nanotechnology. Skyrmionics and related spintronics applications based on thin films with interfacial DMI were recently reviewed by W. Kang et al. [59] and G. Finocchio et al. [60].

For microwave- and magnonics-related applications also the initially discovered skyrmion lattice is intriguing (Fig. 3). However, the metallic layers and bulk metals are not suitable as the damping parameter α is large. Instead, insulators are needed. When aiming at high-power applications insulators particularly in bulk form are key. We thus consider the bulk material Cu₂OSeO₃ with DMI to be the prototypical helimagnet when discussing *magnonics* with chiral magnets.

For our review we put an emphasize on the specific properties and spin dynamics in *periodically* ordered non-collinear spin structures. More than a century ago, periodic arrangements of materials (laminated medium) have been identified as a powerful concept to control and manipulate waves in solids [69]. In photonics, periodically modulated dielectrics –so-called photonic crystals– slowed down light [70]. Appropriate lattice constants are on the order of the relevant wavelength. Chiral magnets allow one to follow this powerful concept for wave control and, at the same

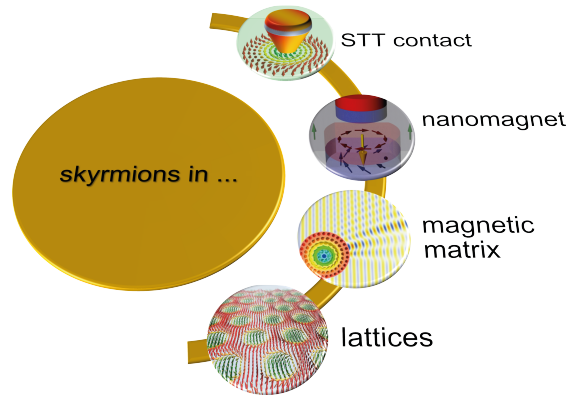


Figure 3. Four different scenarios in which skyrmions have been realized so far. All four scenarios have implications for magnonics, i.e., the control and manipulation of microwave signals by exploiting spin waves. Using spin-transfer torque (STT) a dynamically stabilized skyrmion can be obtained. Second figure from the top: Schematic diagram of the artificial skyrmion lattices and measured magnetic hysteresis loops from Ref. [68] published under CC-BY, rearranged from original.

time, offer unprecedented advantages over materials tailored via e.g. lamination, heteroepitaxy, or patterning. First, the periodic spin structures are formed in a homogeneous material. Assuming a single crystal as a host, wave scattering at potentially rough surfaces and interfaces present in heterogeneous media is avoided. Second, the periodic spin structures are formed spontaneously with lattice constants on the nanoscale that can be below the feature sizes covered by state-of-the-art nanotechnology. This way, chiral magnets provide a *bottom-up* strategy for magnetic nanostructures and magnonic crystals with previously inaccessible lattice constants. Third, metals, semiconductors and insulators (dielectrics) host chiral spin structures. The different classes offer intriguing possibilities to modify the periodic spin structures while processing spin-wave signals. Currents (electric fields) applied to metals (insulators) have already been shown to "gate" the skyrmion lattice. Reconfigurable magnonic crystals are therefore possible with chiral magnets. We note that starting from a perfectly periodic system the intentional incorporation of individual defects such as a photon cavity in photonic crystals or of ensembles of defects such as dopants in semiconductors further enriches the functionality and concept of wave control. We expect the same to hold true for the spin structures discussed in this review. In the discussion we focus mainly on the role of bulk DMI. We note however that surface-induced chiral symmetry breaking in magnetic nanostructures was reported to cause related chiral spatially modulated or localized magnetic structures [71].

This paper is organized as follows. We first review spectroscopy data obtained in the GHz frequency regime on bulk materials hosting the skyrmion lattice phase [72]. So far experiments have been performed at low temperatures as critical temperatures T_c of relevant materials such as MnSi and Cu_2OSeO_3 are below room temperature. Spin wave spectroscopy on the alloy CoZnMn that hosts a skyrmion lattice at room temperature [73] has not yet been published. However, the spin dynamics of Cu_2OSeO_3 have been studied extensively [74, 75, 76, 77, 78, 79, 80, 81, 82, 83]. Recently Mochizuki and Seki have thoroughly reviewed the spin dynamics of

Cu_2OSeO_3 focussing on excitation at the Γ point, i.e., the uniform mode [38, 84, 85]. They discussed in detail magnetoelectric phenomena and the intriguing microwave diode effect occurring in bulk helimagnets [39, 86, 87, 88]. In this paper we review the full band structures of collective spin excitations ranging from zero to large wave vectors k [36, 89] as they are key for applications in magnonics [90]. Our discussion addresses the prototypical insulating ferrimagnet Cu_2OSeO_3 as, at this point it offers the smallest spin-wave damping [91] and has shown the intriguing magnetochiral effects [38, 84, 85]. The properties of Cu_2OSeO_3 particularly motivate the special attention of chiral magnets in magnonics. We then present theoretical considerations how to describe the dynamics in the complex spin structures, and we compare theoretical aspects with experimental findings. In the final section we discuss prospects of spin helices and skyrmions in magnonics considering different scenarios (Fig. 3) ranging from static to dynamically controlled magnonic crystals.

2. Experiments on GHz excitations in materials hosting the skyrmion lattice phase

Spin dynamics in the chiral magnet MnSi was investigated early in the 1970's and 1980's [35, 92], well before the discovery of the skyrmion lattice (SkL) in the same material in 2009 [50]. Since then, the interest in metallic MnSi and in its spin dynamics properties [34] has largely increased. The skyrmions identified in MnSi represent so-called Bloch-type skyrmions as illustrated in Fig. 2. In this case, the spins rotate in a *helical* manner between individual skyrmions. The plane of the SkL is here perpendicular to the applied magnetic field. Later on similar skyrmions were found in other compounds of the same material class with the space group $P2_13$ like Cu_2OSeO_3 [33, 93, 94]. In Cu_2OSeO_3 the copper ions carry each a spin momentum $\frac{1}{2}$ and are arranged in Cu_4 tetrahedra as sketched in Fig. 1 (d) [1]. In each tetrahedron the spins are ordered ferrimagnetically in that one Cu spin [red circles in Fig. 1 (d)] is antiparallel with respect to the three other ones. In the field-polarized ferrimagnetic state each tetrahedron provides total spin $S = 1$ to the saturation magnetization M_s (compare Fig. 2 (d) in Ref. [95]).

Pioneering experiments on characteristic eigenmodes of the SkL phase were performed on the Bloch-type skyrmions by Onose et al. exploring the ferrimagnetic insulator Cu_2OSeO_3 [38]. Using a spectroscopy technique based on a broadband microwave transmission line Onose et al. detected three distinct modes in the few GHz frequency regime, see Fig. 4. The characteristic modes observed for the skyrmion lattice were consistent with an earlier theoretical prediction by Mochizuki [85] and termed clockwise (CW), counterclockwise (CCW) and breathing mode. These modes obey different selection rules: whereas the CW and CCW mode are excited by an oscillating magnetic field H_{AC} located within the plane of the skyrmion lattice, the breathing mode couples to an ac field aligned perpendicular to the plane. The employed technique allowed for the detection of one distinct mode in the field-polarized (FP) phase and two modes labelled as -Q and +Q in the helical (H) and conical (C) phases. In Ref. [38] the selection rules and signal strengths of the different modes suggested an excitation via the magnetic field components of the microwaves.

Earlier published Raman and far-infrared spectroscopy spectra taken on Cu_2OSeO_3 reported also several resonances [96, 97]. They resided at THz frequencies and were observed later also in electron spin resonance experiments performed at high frequencies [98]. An effective Heisenberg model identified such high-frequency

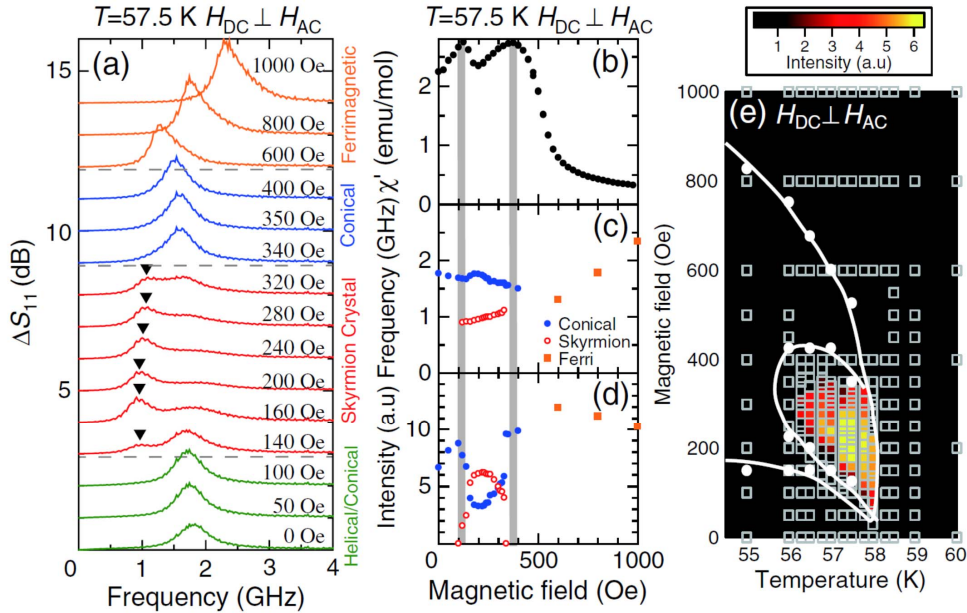


Figure 4. (a) The microwave absorption spectra ΔS_{11} for $H_{DC} \perp H_{AC}$ at various magnetic fields at 57.5 K. (b) Field dependence of the magnetic susceptibility. (c),(d) The (c) frequency and (d) intensity of the magnetic modes of (a). The closed and open circles and closed squares in (c),(d) correspond to the excitations in conical magnetic, skyrmion lattice, and field-polarized states, respectively. (e) The intensity of the counterclockwise (CCW) mode is only finite within the skyrmion lattice phase of the phase diagram. The intensity was determined for temperatures and fields as indicated by the squares. Reprinted figure with permission from Y. Onose et al., Phys. Rev. Lett. 109, 037603, 2012. Copyright (2012) by the American Physical Society.

modes as spin excitations in high-energy magnon bands of Cu_2OSeO_3 [99]. These are determined by the intra-tetrahedron exchange energy [Fig. 1 (d)] [1] that does not have a counterpart in e.g. the prototypical skyrmion-hosting MnSi. The high-energy magnon bands are hence specific to Cu_2OSeO_3 . At the same time, their THz frequencies are far beyond the frequencies that currently play a dominant role in the research field of magnonics and in modern information technology.

In contrast, the low-energy spin excitations explored in the pioneering work by Onose et al. are characteristic for chiral magnets of the $\text{P}2_13$ material class and fall in the technologically relevant regime of GHz frequencies. In Ref. [34] it was shown that the three modes detected in the SkL of Cu_2OSeO_3 and the two modes $-Q$ and $+Q$ in the helical and conical states represent universal excitations of these phases. Schwarze *et al.* explicitly demonstrated that they are shared by the metal MnSi, the semiconductor $\text{Fe}_{0.8}\text{Co}_{0.2}\text{Si}$ and the insulator Cu_2OSeO_3 , see Fig. 5. From material to material, the relevant frequency regime varies (compare frequency values given by $\omega_{c2}^{\text{int}}/2\pi$ in Tab. 1). The frequency values are in the same range as addressed by e.g. YIG-based microwave components.

A member of a different class of skyrmion-hosting materials with a rhombohedral crystal structure and space group $R\bar{3}m$ [100] is GaV_4S_8 . The presence of a magnetic

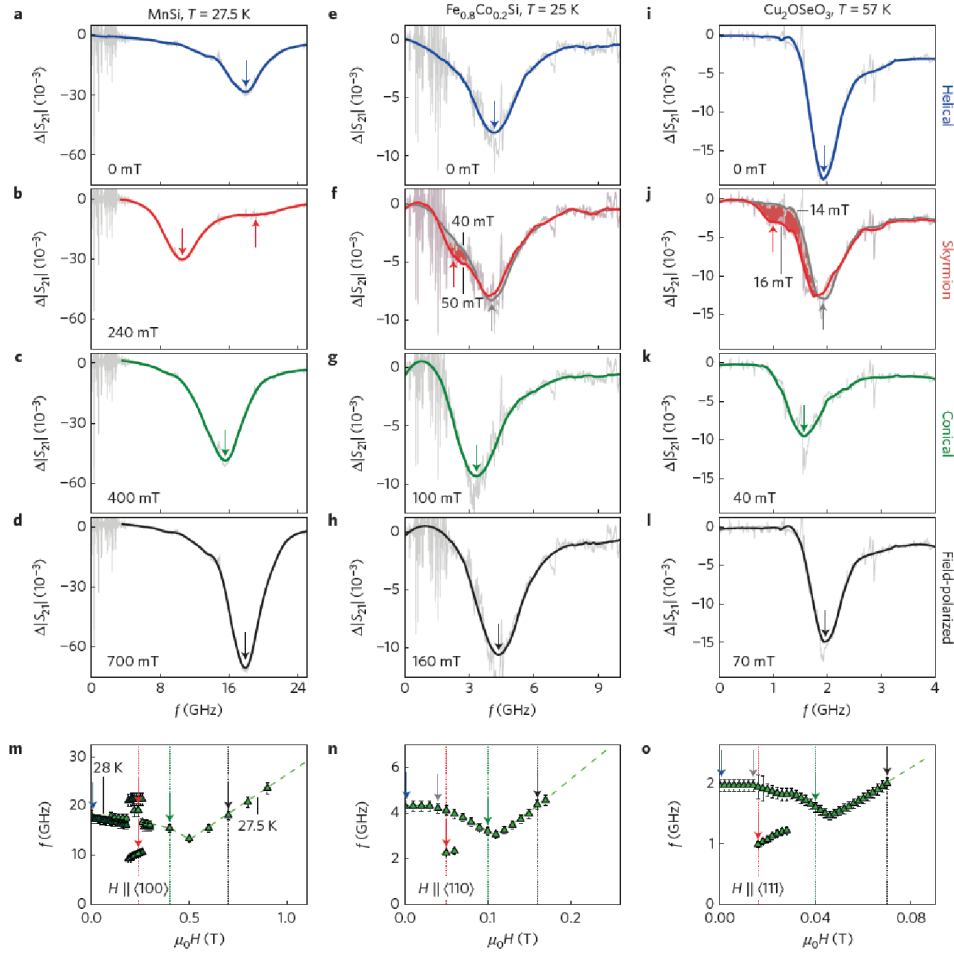


Figure 5. (a) to (l) Spectra obtained on MnSi, Fe_{0.8}Co_{0.2}Si and Cu₂OSeO₃ at various magnetic fields for temperatures just below the relevant T_C . A smoothed curve was added as a guide to the eye. (m) to (o) Corresponding resonance frequencies as a function of magnetic field. Note the different frequency scales. Characteristic resonance frequencies are marked by arrows. Dashed coloured lines indicate field values for which spectra are depicted in the upper rows. The shading between the curves in (f) and (j) highlights the occurrence of a low-frequency mode. Reprinted by permission from Macmillan Publishers Ltd, part of Springer Nature: Nature Materials (T. Schwarze *et al.*, Nat. Mater. 14, pages 478 – 483), copyright (2015). Taken from Ref. [34].

skyrmion phase in bulk GaV₄S₈ was recently reported in Ref. [101]. Here, the skyrmion lattice consists of Néel-type skyrmions where the spins rotate in a *cycloid* manner between individual skyrmions. The reduced crystal symmetry in this compound results in uniaxial magnetic anisotropies and favours the plane of the skyrmion lattice to be oriented along the crystallographic [111] direction. GaV₄S₈ shows a similar characteristic set of low-energy spin excitations as the P2₁3 compounds. However, the relatively large magneto-crystalline anisotropy introduces a different hierarchy of resonance frequencies within the skyrmion lattice phase [45, 46].

In the following section, we focus on chiral magnets with P2₁3 crystal symmetry and review the universal aspects of their low-energy collective spin excitations. The universal characteristics allow one to functionalize the spin structures of chiral magnets over a broad frequency regime. In Fig. 5 frequencies range from about 1 to 30 GHz. At the same time, one can exploit magnetic insulators, semiconductors and metals, i.e., the three technologically relevant material classes. The broad range of available conductivities is particularly advantageous when combining magnonics with e.g. charge-based spintronics [14]. We review the theoretical understanding and highlight aspects relevant for magnonics. We cover the energy and wavelength regime that is consistent with on-chip microwave technologies based on transmission lines and coplanar waveguides.

3. Theoretical considerations about spin excitations in chiral magnets

In the following we focus on the low-energy limit where the magnetization field can be treated in the continuum approximation. We neglect amplitude fluctuations and consider only the orientation of the magnetization, $\vec{M}(\vec{r}) = M_s \hat{n}(\vec{r})$, represented by the unit vector \hat{n} and amplitude M_s . Note that, e.g., MnSi and FeGe are itinerant chiral magnets where M_s possesses a residual magnetic field dependence. Moreover, Cu₂OSeO₃ is a ferrimagnet, for which M_s and $\hat{n}(\vec{r})$ effectively represent the size and orientation of the ferrimagnetic moment, respectively. Intratetrahedron spin excitations involving the strong exchange interactions J_s^{FM} and J_s^{AF} [Fig. 1 (d)] are not considered. The magnetization field \hat{n} is governed by the free energy functional $F = F_0 + F_{\text{dip}} + F_{\text{aniso}}$. In the cubic chiral magnets, the first part $F_0 = \int d\vec{r} \mathcal{F}_0$ possesses the density

$$\mathcal{F}_0 = A(\partial_\alpha \hat{n}_i)^2 + D\hat{n}(\vec{\nabla} \times \hat{n}) - \mu_0 M_s \vec{H} \hat{n} \quad (1)$$

where $\alpha, i = 1, 2, 3$ and summation over repeated indices is implied. A is the exchange stiffness constant, D denotes the strength of the Dzyaloshinskii-Moriya interaction, and \vec{H} is the applied magnetic field. The sign of D depends on the chirality of the atomic crystal structure; here, we assume $D > 0$ resulting in right-handed chiral magnetic structures. In general, the sign of D depends on the chirality of the underlying atomic crystal structure. The crystal chirality however not necessarily corresponds to the magnetic chirality. It was found that a right-handed crystal chirality for MnSi and MnGe leads to a right-handed magnetic chirality, whereas for FeSi and FeGe it results in a left-handed magnetic chirality [102, 103, 104, 105]. For sufficiently small applied fields, the competition between the exchange interaction and the DMI stabilizes spatially modulated textures with a typical wavevector given by $Q = D/(2A)$ [Fig. 2 (b) and (c)]. The DMI can also be expressed $\hat{n}(\nabla \times \hat{n}) = \hat{n}^T (-i\vec{\mathbf{L}}\vec{\nabla})\hat{n}$ in terms of the spin-1 operator $\vec{\mathbf{L}} = (\mathbf{L}^1, \mathbf{L}^2, \mathbf{L}^3)$ defined by the antisymmetric tensor

$$\mathbf{L}_{ij}^\alpha = -i\varepsilon_{ij\alpha}, \quad (2)$$

which is the generator of rotations. It fulfils the spin-1 algebra $[\mathbf{L}^\alpha, \mathbf{L}^\beta] = i\varepsilon_{\alpha\beta\gamma}\mathbf{L}^\gamma$ and $\vec{\mathbf{L}}^2 = 2\mathbf{1}$.

The second part comprises the dipolar interaction

$$F_{\text{dip}} = \frac{\mu_0 M_s^2}{2} \int d\vec{r} d\vec{r}' \hat{n}_i(\vec{r}) \chi_{\text{dip},ij}^{-1}(\vec{r} - \vec{r}') \hat{n}_j(\vec{r}'). \quad (3)$$

The Fourier transform of the susceptibility $\chi_{\text{dip},ij}^{-1}(\vec{k})$ depends on the relative amplitude of the wavevector compared to the inverse linear size of the macroscopic sample L . For large wavevectors $|\vec{k}| \gg 1/L$, it is given by $\chi_{\text{dip},ij}^{-1}(\vec{k}) = \vec{k}_i \vec{k}_j / k^2$. For small wavevectors $|\vec{k}| \ll 1/L$, it is determined by the demagnetization factor N_{ij} of the sample $\chi_{\text{dip},ij}^{-1}(\vec{k}) = N_{ij}$; for an ellipsoidal sample $N_{ij} = N_i \delta_{ij}$ with $N_x + N_y + N_z = 1$. A special situation arises for a highly anisotropic sample like a thin film which we will discuss below.

The third part F_{aniso} contains the magnetic and magnetocrystalline anisotropies. The former might be relevant for thin films whereas the latter is essential for the description of the helix reorientation transition at the first critical field H_{c1} [106]. Here, for simplicity, we will not consider the modifications close to H_{c1} [Fig. 2 (a)] and neglect the magnetocrystalline anisotropies. We will include however the magnetic anisotropy in the discussion of thin films. In Tab. 2 we summarize parameters that are relevant for the bulk materials and their free energy functional.

The equilibrium magnetization profile $\hat{n}_{\text{eq}}(\vec{r})$ is obtained by minimizing the free energy functional and solving the resulting Euler-Lagrange equations. This also includes certain boundary conditions that must be fulfilled at the surfaces of the sample. From the part in Eq. (1), the following boundary conditions arise [107, 108]

$$\hat{s} \vec{\nabla} \hat{n} - Q \hat{s} \times \hat{n} \Big|_{\text{boundary}} = 0 \quad (4)$$

where \hat{s} is the unit vector orthogonal to the sample boundary. Note that the Dzyaloshinskii-Moriya interaction leads to an effective "pinning" of the spins at the boundary. We will not consider explicit boundary terms in the free energy functional which might modify Eq. (4). The effect due to Eq. (4) is negligible for bulk samples. However, in thin films it becomes important for the equilibrium magnetization and magnon spectrum as will be discussed in sect. 4.6.1.

The DMI favors spatially modulated textures so that $\hat{n}_{\text{eq}}(\vec{r})$, in general, will depend on the spatial coordinate \vec{r} . In the linear spin-wave approximation, the magnon modes are obtained by expanding the energy functional around the equilibrium state. For this purpose, we introduce the local orthonormal frame $\hat{e}_i(\vec{r}) \hat{e}_j(\vec{r}) = \delta_{ij}$ with $\hat{e}_3 = \hat{n}_{\text{eq}}$ and $\hat{e}_1 \times \hat{e}_2 = \hat{e}_3$. The spin excitations will be parametrized by the complex wavefunction ψ in a standard fashion

$$\hat{n} = \hat{e}_3 \sqrt{1 - 2 \frac{g\mu_B}{M_s} |\psi|^2} + \sqrt{\frac{g\mu_B}{M_s}} (\psi \hat{e}_+ + \psi^* \hat{e}_-) \quad (5)$$

where $\hat{e}_{\pm} = \frac{1}{\sqrt{2}}(\hat{e}_1 \pm i\hat{e}_2)$. The factor $\frac{g\mu_B}{M_s}$ is introduced so that the product $|\psi|^2$, representing the probability density of magnons, possesses the units of inverse volume. The equation of motion for the magnetization [4] reads $\partial_t \hat{n} = -\gamma \hat{n} \times \vec{B}$ with $\gamma = g\mu_B/\hbar > 0$ and the effective magnetic field $\vec{B} = -\frac{1}{M_s} \frac{\delta F}{\delta \hat{n}}$. Expanding it up to linear order in the magnon wavefunction, we obtain the effective wave equation for the magnon modes that we discuss for various cases in the following. We show that in general the $U(1)$ symmetry associated with the phase of the ψ wavefunction is broken. This reflects the fact that spin angular momentum carried by the magnons is not conserved because of spin-orbit coupling, dipolar interactions and the textured magnetization. For this reason, we introduce the spinor $\vec{\Psi}^T = (\psi, \psi^*)$ whose wave equation has the form

$$i\hbar\tau^z \partial_t \vec{\Psi}(\vec{r}, t) = \mathcal{H} \vec{\Psi}(\vec{r}, t) \quad (6)$$

Table 2. Experimental quantities in terms of the theoretical parameters A , D , and M_s of Eq. (1).

pitch vector	$Q = \frac{D}{2A}$
spin wave stiffness	$\mathcal{D} = \frac{2Ag\mu_B}{M_s}$
critical field energy	$g\mu_0\mu_B H_{c2}^{\text{int}} = \hbar\omega_{c2}^{\text{int}} = \mathcal{D}Q^2 = \frac{D^2 g\mu_B}{2AM_s}$
susceptibility of the conical helix	$\chi_{\text{con}}^{\text{int}} = \frac{M_s}{H_{c2}^{\text{int}}} = \frac{2A\mu_0 M_s^2}{D^2}$

where τ^z is a Pauli matrix and the Bogoliubov–deGennes Hamiltonian \mathcal{H} is a 2×2 matrix operator. This Hamiltonian is constant in time so that we can limit ourselves to the solution of the stationary wave equation, $(\hbar\omega\tau^z - \mathcal{H})\vec{\Psi}(\vec{r}, \omega) = 0$, for the Fourier transform, $\vec{\Psi}(\vec{r}, t) = \int \frac{d\omega}{2\pi} e^{-i\omega t} \vec{\Psi}(\vec{r}, \omega)$. The eigenfrequencies of Eq. (6) come in pairs $\pm\omega$ due to the symmetry of \mathcal{H} , and we focus in the following discussion mostly on the positive eigenfrequencies. It is also convenient to introduce the retarded matrix Green’s function

$$(\hbar(\omega + i0)\tau^z - \mathcal{H})g(\vec{r}, \vec{r}'; \omega) = \delta(\vec{r} - \vec{r}'). \quad (7)$$

The retarded dynamical magnetic susceptibility is then given by

$$\chi_{ij}(\vec{r}, \vec{r}'; \omega) = -g\mu_B\mu_0 M_s (\hat{e}_i^+(\vec{r}), \hat{e}_i^-(\vec{r})) g(\vec{r}, \vec{r}'; \omega) \begin{pmatrix} \hat{e}_j^-(\vec{r}') \\ \hat{e}_j^+(\vec{r}') \end{pmatrix} \quad (8)$$

The prefactor is chosen such that the projection of the spatial Fourier transform $\hat{H}_i \hat{H}_j \chi_{ij}(\vec{k}, \vec{k}'; \omega)$ with $\hat{H} = \vec{H}/H$ reduces to the static dimensionless susceptibility $\chi = \partial M / \partial H$ for $\omega = 0$ and $\vec{k}, \vec{k}' \rightarrow 0$. The imaginary part of Eq. (8) describes dissipation, and it is directly accessible in microwave absorption measurements as well as neutron scattering experiments.

3.1. Magnon excitations of the field-polarized state

We revisit spin-wave excitations in the field-polarized regime of a large bulk sample [denoted by FP in Fig. 2(a)]. A large magnetic field $H > H_{c2}$ is assumed to be applied along the z -axis, $\vec{H} = H\hat{z}$. The magnetization is polarized so that $\hat{n}_{\text{eq}} = \hat{z}$. In this case, the local dreibein can be chosen to be independent of position, e.g., $\hat{e}_1 = \hat{x}$ and $\hat{e}_2 = \hat{y}$. The magnon Hamiltonian is then given by $\mathcal{H} = \mathcal{H}_0 + \mathcal{H}_{\text{dip}}$ where \mathcal{H}_0 derives from Eq. (1) and reads

$$\mathcal{H}_0 = \mathcal{D}(-1\vec{\nabla}^2 - i2Q\tau^z \hat{z}\vec{\nabla}) + g\mu_B\mu_0 H 1 \quad (9)$$

where we used the stiffness $\mathcal{D} = 2Ag\mu_B/M_s$ (Tab. 2). In order to discuss the influence of the dipolar interaction, it is actually more convenient to switch from real to momentum space, $\mathcal{H}_0(-i\nabla) \rightarrow \mathcal{H}_0(\vec{k})$. In momentum space, the Hamiltonian including the contribution from the dipolar interactions reads

$$\mathcal{H} = \mathcal{D}(1\vec{k}^2 + 2Q\tau^z \hat{z}\vec{k}) + g\mu_B\mu_0 H_{\text{int}} 1 + \frac{g\mu_B\mu_0 M_s}{2k^2} \begin{pmatrix} k_+ k_- & k_-^2 \\ k_+^2 & k_+ k_- \end{pmatrix} \quad (10)$$

where $H_{\text{int}} = H - N_z M_s$ is the internal field, and we introduced $k_{\pm} = k_x \pm ik_y$. The eigenfrequencies of the magnon spectrum then follow straightforwardly from solving

the eigenvalue equation (6) and are given by $\pm\omega(\pm\vec{k})$ with

$$\hbar\omega(\vec{k}) = 2\mathcal{D}Qk_z + \sqrt{(\mathcal{D}k^2 + g\mu_B\mu_0 H_{\text{int}}) \left(\mathcal{D}k^2 + g\mu_B\mu_0 H_{\text{int}} + \frac{g\mu_B\mu_0 M_s k_{\perp}^2}{k^2} \right)}. \quad (11)$$

where $\vec{k}_{\perp} = (k_x, k_y, 0)$ and $k = |\vec{k}|$. The second term with the square root corresponds to the Herring-Kittel formula for a ferromagnet [109]. The DMI gives rise to the additional first term and leads to a shift of the dispersion along k_z , i.e., the direction in momentum space singled out by the magnetic field.

In particular, for vanishing perpendicular momentum, $\vec{k}_{\perp} = 0$, the dispersion reduces to a shifted parabola $\hbar\omega(k_z) = \mathcal{D}(k_z + Q)^2 + g\mu_B\mu_0 H_{\text{int}} - \mathcal{D}Q^2$. As a consequence, the magnon dispersion $\omega(k_z)$ is not symmetric with respect to k_z . This implies, for example, a finite group velocity $\partial_{k_z}\omega(k_z) \rightarrow 2\mathcal{D}Q$ in the limit of small $k_z \rightarrow 0$ resulting in nonreciprocal spin wave propagation at small wavevectors. This group velocity is positive for a right-handed DMI as considered here. In case of a left-handed DMI, the momentum shift would be in the opposite direction leading to a negative group velocity. Nonreciprocal spin wave propagation was recently explored for Cu_2OSeO_3 [110]. The DMI-induced term in Eq. (11) also results in an asymmetry in the dynamic susceptibility with respect to k_z . Introducing the spin-flip contributions for the dynamic susceptibility of Eq. (8), $\chi_{\pm\mp}(k_z, \omega) = \hat{e}_i^{\mp} \chi_{ij}(k_z, \omega) \hat{e}_j^{\pm}$, we obtain for its imaginary parts at $k_{\perp} = 0$

$$\chi''_{\pm\mp}(k_z, \omega) = \pm \frac{\pi g\mu_B\mu_0 M_s}{\hbar} \delta(\omega \mp \omega(\pm k_z)). \quad (12)$$

A magnon at a given momentum k_z and energy $\omega(k_z)$ can be absorbed, but, different from a conventional ferromagnet, it cannot be emitted with the same energy as $\omega(-k_z) \neq \omega(k_z)$. This asymmetry in absorption and emission of magnons has been very recently observed in inelastic neutron scattering on MnSi [111].

The energy dispersion $\omega(\vec{k})$, Eq. (11), is minimal for $\vec{k} = Q\hat{z}$ with an energy gap $g\mu_B\mu_0 H_{\text{int}} - \mathcal{D}Q^2$. This gap vanishes at the second critical field H_{c2}^{int} where the transition occurs between the field-polarized (FP) and the conical phase, see Fig. 2(a). The stiffness $\mathcal{D} = g\mu_B\mu_0 H_{c2}^{\text{int}}/Q^2$ is thus determined by the size of the pitch vector Q and the value of H_{c2}^{int} , which are both accessible from independent measurements [37, 44, 112]. We comment on the eigenmodes at zero wavevector attributed to uniform oscillations of the magnetization. In this limit, the Hamiltonian simplifies to

$$\mathcal{H}_{\text{uniform}} = g\mu_B\mu_0 H_1 + g\mu_B\mu_0 M_s \left(-N_z 1 + \frac{N_x + N_y}{2} 1 + \frac{N_x - N_y}{2} \tau^x \right). \quad (13)$$

For the field-polarized phase, the eigenfrequencies have the form of the well-known Kittel mode [4, 113]

$$\hbar\omega = g\mu_B\mu_0 \sqrt{(H + (N_x - N_z)M_s)(H + (N_y - N_z)M_s)}. \quad (14)$$

The uniform mode within a sample of large size is thus not affected by the DMI.

3.2. Magnon excitations of the helical spin structure

When the magnetic field H is lowered below H_{c2} , the field-polarized state becomes unstable with respect to the formation of a conical spin helix. It is characterized by a helix axis that is aligned with the magnetic field. The conical helix is realized in the chiral magnets within the field range between H_{c1} and H_{c2} . If the field is lowered below

H_{c1} the helix might reorient its axis from the field direction into a crystallographic high-symmetry direction, either $\langle 111 \rangle$ or $\langle 100 \rangle$ depending on the material [106]. This reorientation has its origin in the magnetocrystalline anisotropies F_{aniso} . If the field is applied along the favoured crystallographic direction then $H_{c1} = 0$ in case of high-field cooling. In the following, we neglect these anisotropies and the associated complexities arising from the reorientation transition close to H_{c1} . We limit ourselves to the spin waves in the presence of a conical helix configuration. Here, we consider the situation of a bulk sample. Thin films will be discussed in section 4.6.1.

3.2.1. Spin-waves of the magnetic helix in bulk samples: finite wavevectors The conical helix configuration for a magnetic field applied along the z -axis is given by

$$\hat{n}_{\text{helix}}(z) = \sin \theta e^{-iQz\mathbf{L}^z} \hat{x} + \cos \theta \hat{z} = \begin{pmatrix} \sin \theta \cos(Qz) \\ \sin \theta \sin(Qz) \\ \cos \theta \end{pmatrix} \quad (15)$$

It consists of a homogeneous part pointing along the magnetic field direction and a helical part that rotates as a function of the z -coordinate within the plane perpendicular to the field. The helical part is favored by the DMI and can be generated with the help of the z -component of the spin-1 operator $\bar{\mathbf{L}}$ introduced in Eq. (2).

Plugging this Ansatz into the free energy functional and minimizing with respect to the cone angle θ one finds $M_s \cos \theta = \chi_{\text{con}} H = \chi_{\text{con}}^{\text{int}} H_{\text{int}}$ with the susceptibility $\chi_{\text{con}}^{-1} = (\chi_{\text{con}}^{\text{int}})^{-1} + N_z$. We assume here that the z -axis coincides with a principal axis of the sample characterized by the demagnetization factor N_z . The internal susceptibility is given by $\chi_{\text{con}}^{\text{int}} = \mu_0 M_s^2 / (2A Q^2)$. On the mean-field level, the differential susceptibility $\partial M / \partial H = \chi_{\text{con}}$ is thus expected to be constant within the conical phase. This is indeed observed approximately in chiral magnets except for relatively high temperatures close to T_c [114]. The experimentally determined value of the susceptibility $\chi_{\text{con}}^{\text{int}}$, see Table 1, provides an important combination of parameters that will enter the spin-wave spectrum. Moreover, at the second critical field H_{c2} the angle $\theta = 0$ so that $\chi_{\text{con}}^{\text{int}} H_{c2}^{\text{int}} = M_s$ which is consistent with the result of section 3.1.

The helix possesses the continuous screw symmetry. An arbitrary translation of the helix along the z -axis can be compensated by a rotation around the same axis leaving the helix invariant. Mathematically, this is reflected in the fact that $(\mathbf{P}_z - Q\mathbf{L}^z)\hat{n}_{\text{helix}}(z) = 0$ where $\mathbf{P}_z = -i1\partial_z$. An additional discrete symmetry arises in zero field where $\cos \theta = 0$. In this case, the helix is also invariant with respect to a π rotation of real and spin space around the x -axis. These symmetries will be reflected in specific properties of the spin wave excitations as discussed below.

In the conical helix phase, the magnon Hamiltonian deriving from the exchange free energy density \mathcal{F}_0 of Eq. (1) reads [37, 115]

$$\mathcal{H}_0 = \mathcal{D}[-1\vec{\nabla}^2 - i2\tau^z Q\hat{n}_{\perp}(z)\vec{\nabla} + \frac{Q^2 \sin^2 \theta}{2}(1 - \tau^x)]. \quad (16)$$

The magnetic helix gives rise to a periodic potential, $\hat{n}_{\perp}(z) = (\sin \theta \cos(Qz), \sin \theta \sin(Qz), 0)$, for the magnons along the z -direction. The periodic potential leads to Bragg scattering that opens gaps in the energy spectrum and results in magnon bands with different index $n = 0, 1, 2, 3, \dots$. In accordance with Bloch's theorem, the spin wave spectrum $\omega_n(\vec{k})$ is periodic $\omega_n(\vec{k} + m\vec{Q}) = \omega_n(\vec{k})$ for any $m \in \mathbb{Z}$ with $\vec{Q} = Q\hat{z}$. In real space, relevant periodicities $2\pi/Q$ are on the order of 20 to 70 nm for the materials listed in Tab. 1.

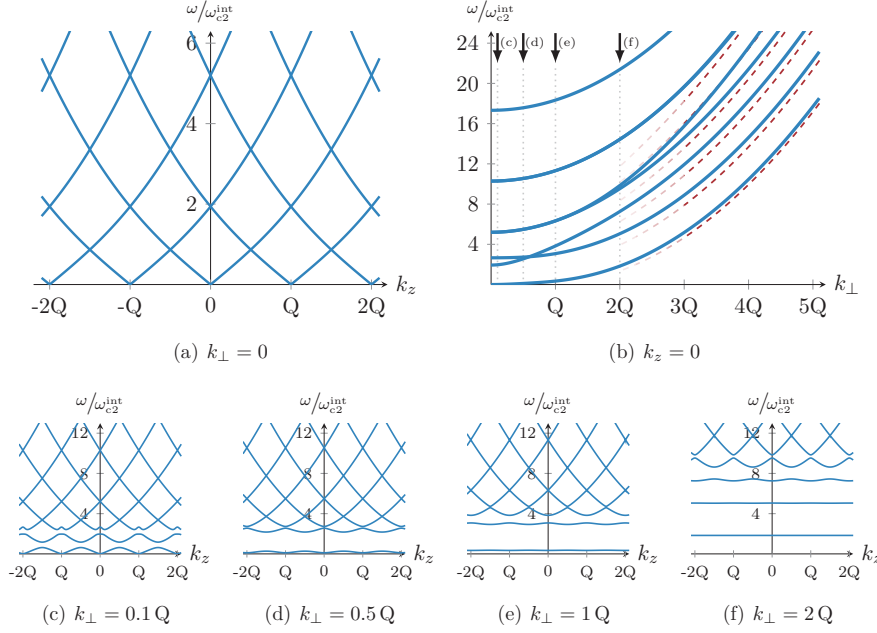


Figure 6. Magnon spectrum in the presence of a helix with cone angle $\theta = \pi/2$ corresponding to zero magnetic field with the value $\chi_{\text{con}}^{\text{int}} = 1.76$ of Cu_2OSeO_3 . Bragg scattering off the helix gives rise to a magnon band structure as a function of wavevector k_z along the helix axis. Spectrum for (a) $\vec{k}_\perp = 0$ of Eq. (19) in the extended zone scheme and (b) $k_z = 0$. The red dashed lines corresponds to the asymptotics of Eq. (21). Arrows indicate cuts shown in the next panels. Panel (c) - (f) illustrate the opening of band gaps for increasing values of $k_\perp = |\vec{k}_\perp|$ and the emergence of flat dispersionless magnon bands. In panel (c) the little bump of the third band close to zone center is attributed to dipolar interactions.

The wave equation is in general not diagonal in momentum space. The full stationary equation including the dipolar interactions reads

$$\begin{aligned}
 & -g_0^{-1}(\omega, \vec{k}) \vec{\Psi}_\omega(\vec{k}) + V(\vec{k}) \vec{\Psi}_\omega(\vec{k} - \vec{Q}) + V^*(\vec{k}) \vec{\Psi}_\omega(\vec{k} + \vec{Q}) \\
 & + \sum_{\substack{\alpha, \beta = -1, 0, 1, \\ \alpha \neq \beta}} \mathcal{H}_{\text{dip}}^{\alpha\beta}(\vec{k} - \alpha\vec{Q}) \Psi_\omega(\vec{k} - (\alpha - \beta)\vec{Q}) = 0.
 \end{aligned} \quad (17)$$

The periodic potential of Eq. (16) leads to the off-diagonal potential $V(\vec{k}) = \mathcal{D}Qk_- \sin\theta\tau^z$ with $k_\pm = k_x \pm ik_y$. The diagonal part is summarized in the Green function

$$-g_0^{-1}(\omega, \vec{k}) = -\hbar\omega\tau^z + \mathcal{D}[1\vec{k}^2 + \frac{Q^2 \sin^2 \theta}{2}(1 - \tau^x)] + \sum_{\alpha=-1, 0, 1} \mathcal{H}_{\text{dip}}^{\alpha\alpha}(\vec{k} - \alpha\vec{Q}) \quad (18)$$

The contribution of the dipolar interaction (3) leads to the terms $\mathcal{H}_{\text{dip}}^{\alpha\beta}$ whose explicit form is given in Appendix A. If the magnon only possesses a momentum along the z -direction, i.e., the direction of the helix, $\vec{k} = k_z \hat{z}$, the problem simplifies considerably. In this case, magnon gaps do not exist in the spectrum because the Fourier transform of the periodic potential, $V(\vec{k})$, vanishes, so that one is left with the empty lattice model for spin waves [21]. The vanishing of Bragg scattering in this limit is attributed

to the continuous screw symmetry of the helix. The spectrum can then be obtained exactly and reads

$$\hbar\omega(k_z) = \mathcal{D}|k_z| \sqrt{k_z^2 + (1 + \chi_{\text{con}}^{\text{int}})Q^2 \left(1 - \left(\frac{H_{\text{int}}}{H_{c2}^{\text{int}}}\right)^2\right)} \quad (19)$$

in the extended zone scheme where the term $\chi_{\text{con}}^{\text{int}}$ arises due to the dipolar interaction, and $H_{\text{int}}/H_{c2}^{\text{int}} = H/H_{c2}$.

In the other limit of large perpendicular momenta $|\vec{k}_{\perp}| \gg Q$ with $\vec{k}_{\perp}\hat{z} = 0$, the dipolar interaction and the last term in Eq. (16) can be effectively neglected. The wave equation for the partial Fourier transform $\vec{\Psi}_{\vec{k}_{\perp},\omega}(z)$ then reduces to

$$\hbar\omega\tau^z \vec{\Psi}_{\vec{k}_{\perp},\omega}(z) \approx \mathcal{D}[1(\vec{k}_{\perp}^2 - \partial_z^2) - i2\tau^z Q|\vec{k}_{\perp}| \sin\theta \cos(Qz - \alpha)] \vec{\Psi}_{\vec{k}_{\perp},\omega}(z) \quad (20)$$

with $\vec{k} = |\vec{k}_{\perp}|(\cos\alpha, \sin\alpha, 0)$. It describes a particle with quadratic dispersion in a periodic cosine potential. This wave equation can be identified with the *Mathieu equation*. Interestingly, the strength of the periodic potential can be tuned by the size of the perpendicular momentum \vec{k}_{\perp} allowing to tune the band structure from the weak-binding to the tight-binding limit. For very large $|\vec{k}_{\perp}| \gg (n+1)^2 Q/\sin\theta$, the Bragg scattering is so strong that the band with index n is basically flat, i.e., non-dispersive, and the spin waves are localized within the z -direction. In this limit, the periodic cosine potential $\cos(Qz - \alpha)$ can be expanded around its minima. Solving the resulting wave equation one obtains [37, 116]

$$\hbar\omega_n(\vec{k}) \approx \mathcal{D} \left[\vec{k}_{\perp}^2 - 2|\vec{k}_{\perp}|Q \sin\theta + 2Q\sqrt{Q|\vec{k}_{\perp}| \sin\theta} \left(n + \frac{1}{2}\right) - \frac{Q^2}{8}(n^2 + n) \right] \quad (21)$$

where $\sin\theta = \sqrt{1 - (H/H_{c2})^2}$. The third term corresponds to the harmonic oscillator spectrum deriving from oscillations around the minima of the cosine potential. The last term is attributed to the anharmonicity of the potential. The spin wave spectra numerically solved for various values of \vec{k}_{\perp} are shown in Fig. 6.

At the Brillouin zone center close to zero wavevector the energy of the lowest band vanishes. This low-energy spin wave is a Goldstone mode and protected by translational symmetry. Both, at zero magnetic field and in the absence of magnetocrystalline anisotropies F_{aniso} that would break the rotational invariance of the theory, the dispersion of this mode is particularly soft [117, 118],

$$\omega^2 \sim Bk_z^2 + Kk_{\perp}^4. \quad (22)$$

It has the Landau-Peierls form characteristic for lamellar structures where B and K are the elastic constants of compression and splay [119], respectively. Such a mode would lead to a Landau-Peierls instability destroying long-range magnetic order of the conical helix. However, either a magnetic field or small magnetocrystalline anisotropies eventually lead to a k_{\perp}^2 contribution to the right-hand side of Eq. (22) that stabilizes the helimagnetic order [117].

The helimagnon spectrum has been measured in MnSi by inelastic neutron scattering [37, 116]. Kugler *et al.* [37] resolved five helimagnon bands as a function of energy as shown in Fig. 7. Such measurements have been also performed on Cu_2OSeO_3 [1, 40] but here the band structure could not be resolved because the associated energy scale $\mathcal{D}Q^2$ is an order of magnitude smaller than in MnSi.

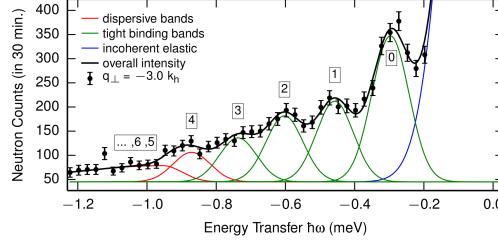


Figure 7. Inelastic neutron scattering on MnSi. Five bands are resolved as a function of energy loss by absorption of helimagnons at $|\vec{k}_\perp| = 3Q$ and $k_z = 0$. Taken from Ref. [37].

3.2.2. Dynamics of the spin helix at zero wavevector: uniform mode According to Eq. (15), the uniform magnetization is given by $\vec{M} = \hat{z}M_s \cos \theta = \hat{z}\chi_{\text{con}}H$. The excitation of the uniform mode results in a dynamic correction to the magnetization, $\delta\vec{M}(t) = \int \frac{d\omega}{2\pi} e^{-i\omega t} \delta\vec{M}(\omega)$ that, in first order in the magnon wavefunction, is determined by

$$\delta\vec{M}(\omega) = \frac{M_s}{V} \int d\vec{r} \sqrt{\frac{g\mu_B}{M_s}} \frac{1}{2} \text{Re} \left\{ (\hat{e}^+(z), \hat{e}^-(z)) \vec{\Psi}(\vec{r}, \omega) \right\} \quad (23)$$

with the volume V . We can perform the real space integral using the representation $\hat{e}_1 = (-\sin(Qz), \cos(Qz), 0)$ and $\hat{e}_2 = (-\cos \theta \cos(Qz), -\cos \theta \sin(Qz), \sin \theta)$ for the vectors $\hat{e}^\pm = \frac{1}{\sqrt{2}}(\hat{e}_1 \pm i\hat{e}_2)$.

Consider first the z -component

$$\delta\vec{M}_z(\omega) = \frac{\sqrt{g\mu_B M_s}}{2\sqrt{2}V} \sin \theta \text{Re} \left\{ i(1, -1) \vec{\Psi}(0, \omega) \right\} \quad (24)$$

where $\vec{\Psi}(0, \omega) = \int d\vec{r} \vec{\Psi}(\vec{r}, \omega)$. It is determined by the magnon wavefunction at zero momentum $\vec{\Psi}(0, \omega)$, which coincides with the Goldstone mode of the helix associated with the breaking of translational symmetry. Its eigenvector is therefore related to the derivative $\partial_z \hat{n}_{\text{helix}}(z) \propto \hat{e}_1$. Comparing this with Eq. (5) identifies the eigenmode $\vec{\Psi}^T(0, \omega) = \frac{1}{\sqrt{2}}(1, 1)$ with eigenfrequency $\omega = 0$. The scalar product $(1, -1)\vec{\Psi}(0, \omega)$ determining $\delta\vec{M}_z$ thus exactly vanishes. So we conclude that in linear order in the spin wave amplitude the mean magnetization does not vary in time along the z -direction, $\delta\vec{M}_z(t) = 0$, within the linear spin-wave approximation considered here.

Resonance frequencies of spin helix modes

The uniform oscillation of the magnetization is therefore confined to the plane in spin space that is orthogonal to the magnetic field,

$$\delta\vec{M}_x(\omega) = \frac{\sqrt{g\mu_B M_s}}{4\sqrt{2}V} \times \quad (25)$$

$$\text{Re} \left\{ i \left((-1 - \cos \theta, -1 + \cos \theta), (1 - \cos \theta, 1 + \cos \theta) \right) \begin{pmatrix} \vec{\Psi}(\vec{Q}, \omega) \\ \vec{\Psi}(-\vec{Q}, \omega) \end{pmatrix} \right\}$$

$$\delta\vec{M}_y(\omega) = \frac{\sqrt{g\mu_B M_s}}{4\sqrt{2}V} \times \quad (26)$$

$$\text{Re} \left\{ \left((1 + \cos \theta, 1 - \cos \theta), (1 - \cos \theta, 1 + \cos \theta) \right) \begin{pmatrix} \vec{\Psi}(\vec{Q}, \omega) \\ \vec{\Psi}(-\vec{Q}, \omega) \end{pmatrix} \right\}$$

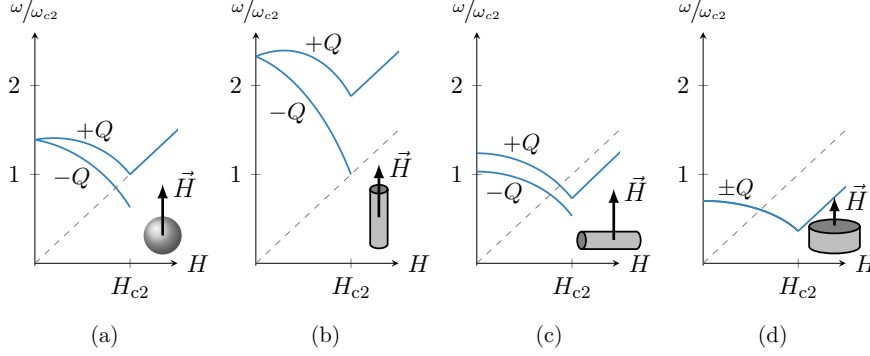


Figure 8. Resonance frequencies of uniform modes in a chiral magnet with $\chi_{\text{con}}^{\text{int}} = 1.76$ corresponding to the value of Cu_2OSeO_3 normalized with respect to $\hbar\omega_{c2} = g\mu_B\mu_0 H_{c2}$. The dc magnetic field \vec{H} is applied along the z -axis and tunes between the conical and field-polarized phase with a phase transition at H_{c2} . The solid line above H_{c2} indicates the position of the Kittel resonance. There are two resonances $\pm Q$ in the conical phase, $H < H_{c2}$, whose frequencies and field dependencies strongly depend on the sample shape: (a) sphere with demagnetization factors $N_x = N_y = N_z = 1/3$, (b) rod with $N_z = 0$ and $N_x = N_y = 1/2$, (c) rod with $N_x = 0$ and $N_y = N_z = 1/2$, (d) thin platelet with $N_z = 1$ and $N_x = N_y = 0$. The dashed line in each panel indicates the resonance frequency in the paramagnetic limit $\omega = g\mu_B\mu_0 H/\hbar$.

where $\vec{\Psi}(\pm\vec{Q}, \omega) = \int d\vec{r} e^{\mp i\vec{Q}\cdot\vec{r}} \vec{\Psi}(\vec{r}, \omega)$. The oscillations within this (x, y) plane are determined by the two components $\vec{\Psi}(\pm\vec{Q}, \omega)$ of the magnon wavefunction. It turns out that these two components are decoupled from the other modes and governed by the wave equation

$$\begin{pmatrix} -g_0^{-1}(\omega, \vec{Q}) & \mathcal{H}_{\text{dip}}^{1,-1}(0) \\ \mathcal{H}_{\text{dip}}^{-1,1}(0) & -g_0^{-1}(\omega, -\vec{Q}) \end{pmatrix} \begin{pmatrix} \vec{\Psi}(\vec{Q}, \omega) \\ \vec{\Psi}(-\vec{Q}, \omega) \end{pmatrix} = \mathbf{0} \quad (27)$$

where the Green function reads explicitly

$$\begin{aligned} -g_0^{-1}(\omega, \pm\vec{Q}) &= -\hbar\omega\tau^z + \mathcal{D}Q^2 \left[1 + \frac{\sin^2\theta}{2}(1 - \tau^x) \right] \\ &+ \chi_{\text{con}}^{\text{int}} \left(\frac{\sin^2\theta}{2}(1 - \tau^x) + \frac{N_x + N_y}{4} ((1 + \cos^2\theta)1 + \sin^2\theta\tau^x \pm \cos\theta\tau^z) \right). \end{aligned} \quad (28)$$

The term in the last line is attributed to the dipolar interaction and, again, its strength is conveniently parametrized by $\chi_{\text{con}}^{\text{int}}$; note that $\mathcal{D}Q^2\chi_{\text{con}}^{\text{int}} = g\mu_B\mu_0 M_s$ (Tab. 2). The off-diagonal parts read

$$\mathcal{H}_{\text{dip}}^{1,-1}(0) = \mathcal{D}Q^2\chi_{\text{con}}^{\text{int}} \frac{N_x - N_y}{4} \left(-\sin^2\theta 1 - i2\cos\theta\tau^y - (1 + \cos^2\theta)\tau^x \right) \quad (29)$$

and $\mathcal{H}_{\text{dip}}^{-1,1}(0) = (\mathcal{H}_{\text{dip}}^{1,-1}(0))^\dagger$. The solution of the 4×4 matrix (27) determines the eigenfrequencies and eigenvectors of the uniform oscillations of the magnetization within the conical helix phase. There are two eigenmodes denoted by $\pm Q$ in the literature [38, 34]. The corresponding positive eigenfrequencies are given by

$$\begin{aligned} \frac{\hbar\omega_{\pm Q}}{g\mu_B\mu_0 H_{c2}} &= \frac{1}{2(1 + N_z\chi_{\text{con}}^{\text{int}})} \left((2 + \chi_{\text{con}}^{\text{int}})(4 + (N_x + N_y)\chi_{\text{con}}^{\text{int}}) \right. \\ &\left. + \hbar^2(-4 + \chi_{\text{con}}^{\text{int}}(-4 - N_y\chi_{\text{con}}^{\text{int}} + N_x(-1 + 2N_y)\chi_{\text{con}}^{\text{int}})) \pm \right. \end{aligned} \quad (30)$$

$$\chi_{\text{con}}^{\text{int}} \left[N_y^2 (2 + \chi_{\text{con}}^{\text{int}} - h^2 \chi_{\text{con}}^{\text{int}})^2 + N_x^2 (2 + (1 + h^2(-1 + 2N_y)) \chi_{\text{con}}^{\text{int}})^2 - 2N_x N_y ((2 + \chi_{\text{con}}^{\text{int}})^2 - 2h^2(2 + \chi_{\text{con}}^{\text{int}})(4 + \chi_{\text{con}}^{\text{int}} + N_y \chi_{\text{con}}^{\text{int}}) + h^4(8 + \chi_{\text{con}}^{\text{int}}(8 + \chi_{\text{con}}^{\text{int}} + 2N_y \chi_{\text{con}}^{\text{int}}))) \right]^{1/2} \Big)^{1/2}$$

where we expressed the energy $\mathcal{D}Q^2 = g\mu_B\mu_0 H_{c2}^{\text{int}}$ in terms of the second critical field $H_{c2} = H_{c2}^{\text{int}}(1 + N_z \chi_{\text{con}}^{\text{int}})$, and we abbreviated $h = \cos\theta = H/H_{c2} = H_{\text{int}}/H_{c2}^{\text{int}}$. This result was first presented in Ref. [34] where the formula is given in terms of the susceptibility $\chi_{\text{con}}^{-1} = (\chi_{\text{con}}^{\text{int}})^{-1} + N_z$.

For generic sample shapes eigenfrequencies of modes +Q, -Q for $H < H_{c2}$ as well as the uniform Kittel mode of Eq. (14) for $H > H_{c2}$ in the FP phase are shown in Fig. 8. For $N_x = N_y \neq 0$ the modes +Q and -Q are found to be degenerate at zero field $H = 0$ and to split when H approaches H_{c2} [Fig. 8 (a) and (b)]. In Fig. 8 (c) the modes +Q and -Q exhibit different frequencies for all H when $N_x \neq N_y$. In the limit of a thin platelet, $N_x = N_y = 0$ and $N_z = 1$, the eigenfrequencies are degenerate for all fields $H < H_{c2}$, see Fig. 8(d). In this limit they are given by Kataoka's formula [89]

$$\hbar\omega_{\pm Q}|_{\text{disc}} = g\mu_B\mu_0 H_{c2}^{\text{int}} \sqrt{1 + (1 + \chi_{\text{con}}^{\text{int}})(1 - h^2)} \quad (31)$$

with $h = H_{\text{int}}/H_{c2}^{\text{int}}$. This formula is consistent with the bulk spectrum of Eq. (19) at $k_z = Q$. The branch in the FP phase is found either above or below the paramagnetic limit (dashed lines) depending on whether the shape anisotropy field adds to or subtracts from the applied field, respectively [4].

Polarization and spectral weights of modes

The eigenvectors of Eq. (27) determine the helicity, i.e., the sense of precessional motion, the polarization and weights of the resonances. The weights as a function of field are shown in Fig. 9. The $\pm Q$ modes have a well-defined helicity provided that they are non-degenerate. The uniform magnetization oscillates counterclockwise for the +Q mode and clockwise for the -Q mode. As a result, the weight of the +Q mode continuously connects to the Kittel mode at the critical field, H_{c2} , because they possess the same helicity, i.e., for both modes the uniform magnetization precesses counterclockwise. In contrast, the weight of the -Q mode vanishes as H_{c2} is approached. Note that in general the helicity of the dynamical precession is determined by the sign of the gyromagnetic ratio. Individual magnetic moments attributed to electrons always precess counterclockwise around a static field and so does the uniform Kittel mode in the field-polarized phase. This is independent of the chirality of the crystal, and, in particular, it remains unaffected by the reversal of the DMI, i.e., by considering a left-handed instead of a right-handed material.

If the modes are degenerate as for $N_x = N_y = 0$, one can always choose a basis of, for example, two circularly polarized degenerate eigenmodes. However, in the generic case of two non-degenerate modes, each of them possesses a distinct polarization and ellipticity. This leads to an interesting dependence of their weights on the orientation \vec{H}_{ac} of a linearly polarized ac field as illustrated in Fig. 9. Both modes are in general elliptically polarized where the axes are defined by the sample shape. We introduce the ellipticity defined by

$$\varepsilon = \text{sign}\{\delta M_x - \delta M_y\} \frac{\sqrt{|\delta M_x^2 - \delta M_y^2|}}{\max\{\delta M_x, \delta M_y\}} \quad (32)$$

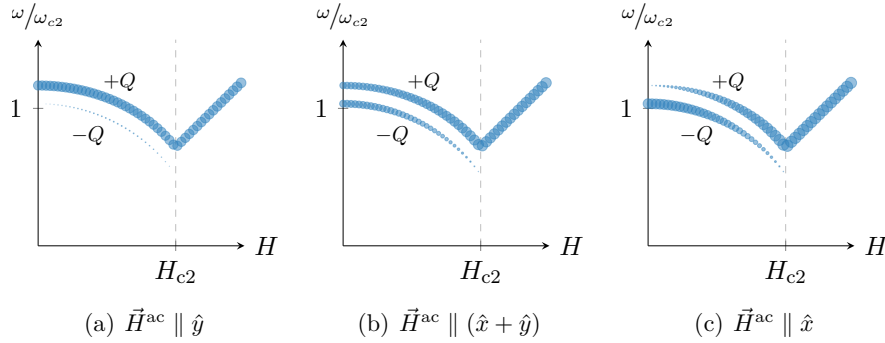


Figure 9. Theoretically evaluated weights (symbol size) of the uniform resonances of the chiral magnet Cu_2OSeO_3 with $\chi_{\text{con}}^{\text{int}} = 1.76$ in the conical and field-polarized phase for a linearly polarized ac magnetic field and different orientations of the linear polarization (a)-(c). The shape is chosen to be rod-like with demagnetization factors $N_x = 0.07$, $N_y = 0.4$, and $N_z = 0.53$ and the dc field is applied along the z -axis. The weights depend on the relative orientation of the rod and the polarization of \vec{H}_{ac} . Generally, the weight of the $-Q$ mode vanishes at H_{c2} while the weight of the $+Q$ mode smoothly connects to the Kittel mode. Note that at $H = 0$ the two modes $\pm Q$ can be selectively addressed by varying the polarization.

where $\delta M_{x,y}$ are the positive amplitudes of the oscillations within the (x, y) plane. We introduce a sign so that $\varepsilon > 0$ if the major axis is aligned with the x -axis and $\varepsilon < 0$ if it is aligned with the y -axis. The ellipticity for the $\pm Q$ modes is shown in Fig. 10 for a specific value of N_z as a function of N_x . Interestingly, we find that at zero field $\vec{H} = 0$ the two modes are generically linearly polarized, i.e., $\varepsilon = \pm 1$.

The linear polarization is related to the π -rotation symmetry of the helix that is present at zero field, see the discussion below Eq. (15). This symmetry is represented by the matrix operator

$$\begin{pmatrix} 0 & 1 \\ 1 & 0 \end{pmatrix} \quad (33)$$

that commutes at $\vec{H} = 0$ with the Hamiltonian, i.e., with the 4×4 matrix of the wave equation (27). As a result, the two eigenmodes $\pm Q$ are also eigenvectors of the matrix (33) with two distinct eigenvalues. Moreover, the amplitudes δM_x and δM_y are determined by the projection of the wavefunction $(\vec{\Psi}^T(\vec{Q}, \omega), \vec{\Psi}^T(-\vec{Q}, \omega))$, see Eq. (25), onto different degenerate subspaces of the π -symmetry operator (33). At zero field, either of the two amplitudes thus vanishes leading to a linear polarization. In less mathematical terms, the π -rotation symmetry ensures that there are always pairs of spins within the helix whose local precessions conspire such that in total only a linear polarization remains. This situation seems to be similar to easy-plane antiferromagnets where the precession of magnetic moments on the two sublattices also combine to yield a linearly polarized uniform mode at antiferromagnetic resonance [4, 120]. In contrast to antiferromagnets, the linear polarization for chiral magnets is however an interplay between DMI and sample shape. Because the relevant energy scale of DMI is orders of magnitude smaller compared to antiferromagnetic exchange interaction, the linearly polarized modes of Cu_2OSeO_3 reside at small frequencies [4].

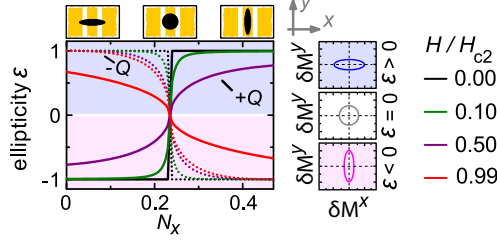


Figure 10. Ellipticity as defined in Eq. (32) of the uniform resonances $\pm Q$ in the conical phase as a function of demagnetization factor N_x at fixed $N_z = 0.53$ and $N_y = 1 - N_x - N_z$ for various magnetic fields and $\chi_{\text{con}}^{\text{int}} = 1.76$ [121]. At zero field $H = 0$, the $\pm Q$ modes are linearly polarized $|\varepsilon| = 1$ for generic sample shapes.

Figure 10 also indicates that the ellipticity of the $+Q$ mode changes sign implying that it changes the major axis of its elliptical polarization as a function of field. Generally, this is expected to occur at the magnetic field

$$\frac{H_+^{\text{circ}}}{H_{c2}} = \frac{2 + \chi_{\text{con}}^{\text{int}}}{\sqrt{(2 + \chi_{\text{con}}^{\text{int}})(2 + (2 - N_z)\chi_{\text{con}}^{\text{int}}) + \sqrt{(1 - N_z)\chi_{\text{con}}^{\text{int}}(2 + \chi_{\text{con}}^{\text{int}})^2(4 + (1 - N_z)\chi_{\text{con}}^{\text{int}})}}} \quad (34)$$

For Cu_2OSeO_3 with $\chi_{\text{con}}^{\text{int}} = 1.76$ and a sample with $N_z = 0.53$ this yields $H_+^{\text{circ}}/H_{c2} \approx 0.76$. At this specific field, the $+Q$ mode is circularly polarized irrespective of the values of the demagnetization factors N_x and N_y .

In the early experiments by Date *et al.* [35] both $\pm Q$ excitation modes were detected on MnSi. Onose *et al.* [38] reported the two modes for Cu_2OSeO_3 (Fig. 4). Finally, Schwarze *et al.* [34] performed microwave resonance experiments on MnSi, Cu_2OSeO_3 and $\text{Fe}_{0.8}\text{Co}_{0.2}\text{Si}$, and found quantitative agreement with the theory reviewed above. The linear polarization of the $\pm Q$ modes in zero field was explored and experimentally confirmed by Stasinopoulos *et al.* [121].

3.3. Magnon excitation of the skyrmion crystal

The Dzyaloshinskii-Moriya interaction not only favours helices but also topological solitons. Within the field-polarized state, a single soliton is generated by the map

$$\hat{n}_{\text{Sk}}(\vec{r}) = e^{i\vec{f}_{\text{Sk}}(\vec{r})\vec{L}\hat{z}} = \begin{pmatrix} -\sin \chi \sin \theta(\rho) \\ \cos \chi \sin \theta(\rho) \\ \cos \theta(\rho) \end{pmatrix} \quad (35)$$

where \vec{L} is the spin-1 operator of Eq. (2) and $\vec{f}_{\text{Sk}}(\vec{r}) = \theta(\rho)\hat{\rho}$ with $\vec{r} = (\rho \cos \chi, \rho \sin \chi, z)$ in cylindrical coordinates and $\hat{\rho} = (\cos \chi, \sin \chi, 0)$. Note that \vec{f}_{Sk} is a conservative vector field and possesses a potential according to $\vec{f}_{\text{Sk}}(\vec{r}) = \vec{\nabla}\Theta_{\text{Sk}}(\rho)$ with $\theta(\rho) = \partial_\rho\Theta_{\text{Sk}}(\rho)$. The function $\theta(\rho)$ obeys the asymptotics $\theta(0) = \pi$ and $\theta(\rho) \rightarrow 0$ as $\rho \rightarrow \infty$. This soliton is translational invariant along the field-direction, i.e., the z -axis, and it varies within the plane perpendicular to the field. In a three dimensional bulk magnet, it defines in fact a string. The soliton carries a finite topological skyrmion number so that it is referred to simply as a skyrmion [Fig. 2 (d)]. The topological skyrmion density within the (x, y) plane is defined by $\rho_{\text{top}} = \frac{1}{4\pi}\hat{n}(\partial_x\hat{n} \times \partial_y\hat{n})$. Integrating the topological density of the texture (35) yields an integer, $\int dx dy \rho_{\text{top}} = -1$. Minimizing the exchange energy of Eq. (1) with the

Ansatz (35), i.e., neglecting the dipolar interactions one obtains an ordinary differential equation that determines the function $\theta(\rho)$, which was first discussed by Bogdanov and Hubert [122]. Importantly, one finds that $\theta(\rho)$ decays exponentially so that the skyrmion is confined to an area that scales approximately as $1/\vec{H}^2$ where \vec{H} is the magnetic field [123].

The magnon scattering off such a single skyrmion will be discussed in section 4.4. Here, we focus on the spin wave excitation of a skyrmion crystal. When it is energetically advantageous to condense skyrmions, they proliferate and form a skyrmion lattice [Fig. 2(e)]. Such a magnetic state is observed in bulk crystals of chiral magnets at intermediate fields and close to the critical temperature [Fig. 2(a)]. A skyrmion crystal state can be generated with the help of the map

$$\hat{n}_{\text{SkX}}(\vec{r}) = e^{i\vec{f}_{\text{SkX}}(\vec{r})\vec{L}\hat{z}} \quad (36)$$

with \vec{L} of Eq. (2). The potential of the conservative vector function $\vec{f}_{\text{SkX}}(\vec{r}) = \vec{\nabla}\Theta_{\text{SkX}}(\vec{r}_{\perp})$ again only varies within the plane perpendicular to the magnetic field, $\vec{r}_{\perp} = (x, y, 0)$. It possesses the periodicity of a two-dimensional hexagonal Bravais lattice L , i.e., $\Theta_{\text{SkX}}(\vec{r}_{\perp}) = \Theta_{\text{SkX}}(\vec{r}_{\perp} + \vec{R}_i)$ for any vector $\vec{R}_i \in L$. If the lattice constant a is large compared to the skyrmion radius, this potential can be approximated to be the sum of individual skyrmion potentials $\Theta_{\text{SkX}}(\vec{r}_{\perp}) \approx \sum_{\vec{R}_i \in L} \Theta_{\text{Sk}}(\vec{r}_{\perp} - \vec{R}_i)$. However, it turns out that the skyrmions are closely packed, and the lattice constant a is in fact comparable to the skyrmion diameter so that Θ_{Sk} is expected to differ from the single-skyrmion solution. In any case, minimization of the free energy (1) with such a type of Ansatz does not yield a smaller energy than the competing conical state of Eq. (15). The phase diagram of Fig. 2 can therefore not be explained on the mean-field level. It was argued in Ref. [124] that fluctuations around the mean-field potential stabilizes the SkL, which was subsequently confirmed by Monte-Carlo simulations [125].

Once the SkL is stabilized the magnon spectrum can be derived on the mean-field level taking into account both contributions, the exchange and the dipolar energies of Eqs. (1) and (3), respectively. However, for practical purposes it is more convenient to relax the constraint of \hat{n} being a unit vector and to work instead within the framework of a linear sigma model. In the following, we present numerical results for the spin wave spectrum of skyrmion crystals in bulk chiral magnets. For computational details we refer the reader to Refs. [34] and [126].

3.3.1. Spin waves of the skyrmion crystal in bulk samples: finite wavevectors The periodicity of the two-dimensional hexagonal skyrmion crystal gives rise to a magnon band structure with a two-dimensional Brillouin zone in the (x, y) plane perpendicular to the applied magnetic field [inset in Fig. 11 (a)]. Figure 11 (a) shows the magnon dispersion for vanishing out-of-plane momentum $k_z = 0$ along particular symmetry directions within the first Brillouin zone for the parameter $\chi_{\text{con}}^{\text{int}} = 0.34$ corresponding to MnSi. Figure 11 (b) shows the spectrum for Cu_2OSeO_3 with $\chi_{\text{con}}^{\text{int}} = 1.76$ yielding a compressed band structure as compared to panel (a). For better comparison, the first 14 bands in (a) and (b) are shown as solid lines and the remaining bands are displayed as dashed lines. Figure 11 (c) shows the complete magnon spectrum of MnSi for wavevectors in the plane of the SkL.

Similarly to the conical helix, the skyrmion crystal breaks translational invariance so that the spectrum possesses a Goldstone mode. This mode arises at the Γ point where the lowest band touches zero energy. Its excitation energy vanishes quadratically

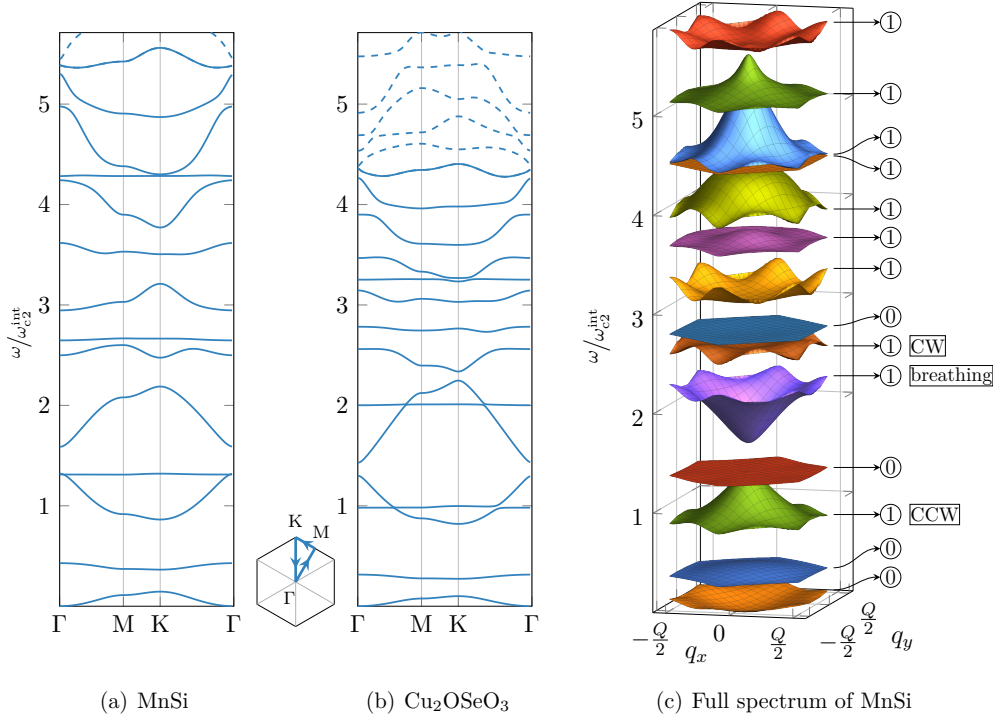


Figure 11. Magnon band structure of the hexagonal skyrmion crystal in chiral magnets within the first Brillouin zone in units of $\hbar\omega_{c2}^{\text{int}} = g\mu_B\mu_0 H_{c2}^{\text{int}}$. The magnon wavenumber is confined to the two-dimensional plane orthogonal to the magnetic field, i.e. $k_z = 0$. Panel (a) and (c) show the spectrum for the parameter $\chi_{\text{con}}^{\text{int}} = 0.34$ corresponding to MnSi and panel (b) for Cu_2OSeO_3 with $\chi_{\text{con}}^{\text{int}} = 1.76$. The inset between (a) and (b) displays the first Brillouin zone. The Chern number of the bands are given on the right-hand side of panel (c). The magnon excitations at the zone center of the 3rd, 5th and 6th band in panel (c) correspond to the uniform CCW, breathing and CW modes, see Figs. 12 and 13.

with momentum, $\omega \sim k^2$, which has been attributed to the topological nature of the skyrmions in Refs. [115, 127].

The non-trivial topology has further consequences. As will be explained in detail in section 4.4, each skyrmion acts like an orbital magnetic field with quantized flux resulting in skew scattering. It is therefore expected that a magnon in a skyrmion crystal experiences this magnetic flux per magnetic unit cell. As a consequence, magnons should occupy Landau levels that are reflected in non-trivial Chern numbers of the band structure [128]. The Chern numbers of the magnon bands for $\chi_{\text{con}}^{\text{int}} = 0.34$ are shown on the right-hand side of Fig. 11(c). We find that for the lowest 14 bands, for which we were able to compute these numbers reliably, most of the bands have a Chern number 1 with a few exceptions, in particular, at low energies where the Chern number is zero. For the parameters of MnSi, the magnon bands are sufficiently well separated allowing for an unambiguous computation. For the parameters of Cu_2OSeO_3 some of the bands come very close rendering the computation of Chern numbers difficult. Up to such ambiguities, the Chern numbers listed in Fig. 11 (c) are consistent with the work of Roldán-Molina *et al.* [129]. The band structures of Fig. 11 will be further

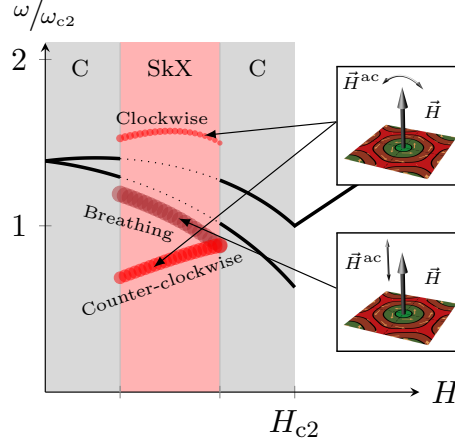


Figure 12. Field dependence of the resonance frequencies of the breathing mode, counterclockwise (CCW) and clockwise (CW) mode – the three uniform resonances of the skyrmion crystal – as expected for a spherical sample of Cu_2OSeO_3 . An ac magnetic field linearly polarized within the skyrmion crystal plane excites both CW and CCW modes where the latter always possesses larger weight as indicated by the size of the dots. The breathing mode possesses an out-of-plane linear polarization. The black solid lines indicate the positions of the resonances of the other phases.

discussed in sect. 4.

3.3.2. Spin waves of the skyrmion crystal in bulk samples: uniform mode Due to the back-folding induced by the periodicity of the skyrmion crystal, there is a multitude of modes present at the Γ point, i.e., at zero wavevector. However, similar to the conical helix, only a few of them are magnetically active and excited by an homogeneously oscillating magnetic field. For the skyrmion crystal, there are three uniform magnetic modes, breathing, CCW and CW mode, first identified theoretically by Mochizuki [85].

The breathing mode possesses a macroscopic dipole moment oscillating out-of-plane, i.e., it is linearly polarized and excited with a longitudinal ac magnetic field (Fig. 12). The size of each skyrmion in the crystal performs an oscillating motion as illustrated in Fig. 13. Its resonance frequency decreases with magnetic field similar to the $\pm Q$ modes of the adjacent conical phase. In case of phase coexistence within the sample, the breathing mode can be distinguished from the former by its polarization which is orthogonal to the ones of the $\pm Q$ modes.

The uniform magnetization of the CCW and CW modes oscillates counterclockwise and clockwise, respectively, in the plane of the skyrmion crystal. They are excited with an in-plane ac field. These modes are in general elliptically polarized along different axes that are determined by the sample shape. Their ellipticity however varies only slightly within the limited magnetic field range where the skyrmion crystal is found [126]. Generally, an ac field linearly polarized within the plane excites both modes but the CCW mode always has a larger weight (Fig. 12). Whereas the resonance frequency of the CCW increases with field, the CW frequency only depends weakly on the magnetic field consistent with experimental observations [34, 38].

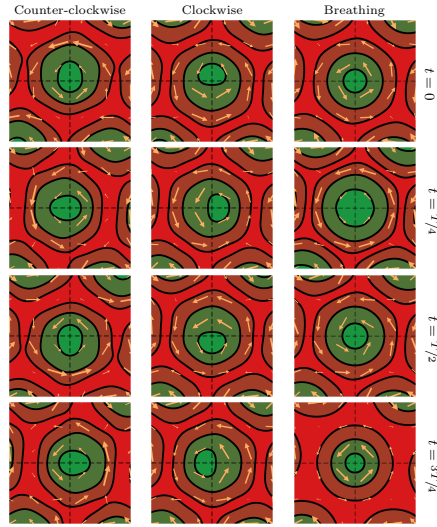


Figure 13. Evolution of the magnon wavefunction in real space as a function of time for the three uniform resonance modes of the skyrmion crystal. T is the respective time period. The dc magnetic field points out of the image plane. The in-plane components of the magnetization are shown by amber colored arrows while the out-of-plane component is represented by a contour plot where green corresponds to the magnetization pointing anti-parallel to the dc field, i.e., into the plane, and red indicates magnetization pointing out of plane.

4. Prospects and challenges

After reviewing the spin wave excitations of the various magnetic phases in bulk samples of cubic chiral magnets, we discuss future research avenues as well as challenges for magnonics applications in the following.

4.1. Magnonics with cubic chiral magnets

The chiral magnets with bulk DMI provide strikingly new characteristics in view of magnonic crystals and manipulation of spin waves in solids. The DMI-induced spin helix introduces a periodic potential [Eq. (16)] for magnons that leads to backfolding of spin-wave dispersion relations and Brillouin zone boundaries at half the pitch vector Q (Fig. 6). For Cu_2OSeO_3 the intrinsic pitch length that defines the periodicity of the helix amounts to about 60 nm. Thereby magnonic crystal equivalent band structures are formed in a bottom-up strategy avoiding any top-down nanopatterning that typically introduces roughness and inhomogeneous broadening. In addition, in the helical phase, the band structure changes qualitatively as a function of momentum \vec{k}_\perp transverse to the helix axis, see Fig. 6. For large $|\vec{k}_\perp| \gg Q$, the lowest bands become flat implying that the magnons are localized along the helix axis and only propagate transverse to it, i.e., the spin waves experience a channeling effect. Channeling of spin waves is well known for two-dimensional magnonic crystals made from antidot lattices [130, 131]. In their case the inhomogeneous demagnetization field induced by in-plane magnetic fields creates narrow channels that are perpendicular with respect to the applied field direction. In the helical or conical phase, spin waves are localized within planes perpendicular to the pitch vector \vec{Q} . The orientation of the latter can

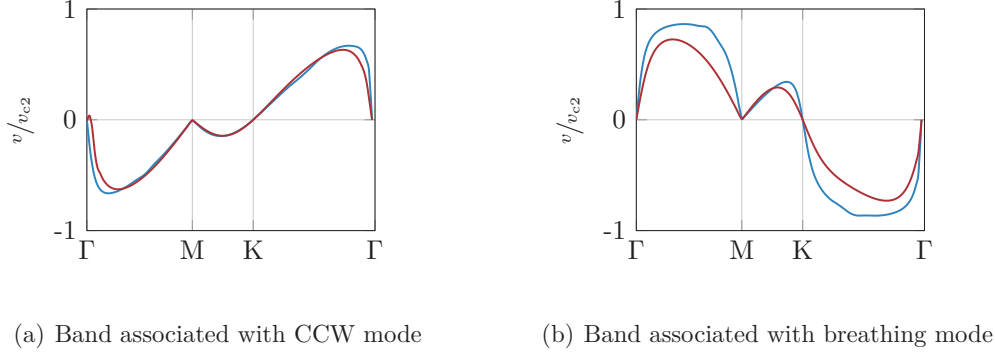


Figure 14. Magnon group velocity $v = \partial_k \hbar \omega_{\vec{k}}$ along certain directions within the first Brillouin zone of the skyrmion lattice for MnSi (blue solid line) and Cu_2OSeO_3 (red solid line). The two bands are shown that contain at their respective Γ point the magnetically active breathing and CCW modes, see Fig. 11. The velocities are on the order of $v_{c2} = \omega_{c2}^{\text{int}}/Q = g\mu_B\mu_0 H_{c2}^{\text{int}}/(\hbar Q)$.

be manipulated with an applied magnetic field allowing to control the channeling. Future research might explore the multitude of tuneable parallel channels in view of spin wave multiplexer on the nanoscale.

Within the phase of the skyrmion lattice, the magnetic Brillouin zone becomes two-dimensional and also contains dispersive magnon bands. The dispersion is particularly pronounced for the magnetically active bands associated with the breathing and CCW modes at their respective Γ point, see Fig. 11. Their group velocities $v = \partial_k \hbar \omega_{\vec{k}}$ along certain lines within the two-dimensional Brillouin zone are shown in Fig. 14. The velocities are on the order of $v_{c2} = \hbar \omega_{c2}^{\text{int}}/(\hbar Q)$ which corresponds to $v_{c2} \approx 300$ m/s for MnSi and $v_{c2} \approx 140$ m/s for Cu_2OSeO_3 . The band structures of Fig. 11 feature well separated bands and pronounced forbidden frequency gaps. To obtain complete band gaps for top-down fabricated magnonic crystals nanoscale lattice constants would be needed that introduce Bragg scattering for exchange-dominated spin waves. Such small lattice constants are however technologically challenging.

It has been already demonstrated that the SkL in Cu_2OSeO_3 can be manipulated with an electric field due to magnetoelectric coupling [79, 132, 84]. Electric-field controlled magnetic crystals based on SkLs should thus be possible. Technologically electric field control is most advantageous as electric fields can be confined very precisely and allow for a low power consumption. At the same time, the SkL might be exploited as either a resonant or non-resonant magnonic grating coupler if integrated to a coplanar waveguide [11, 133]. Relevant wavelengths for emitted spin waves are on the order of the inverse of reciprocal lattice vectors G [11, 133]. In case of an SkL we assume for the smallest non-zero reciprocal lattice vector $G = Q$ leading to spin-wave wavelengths $\lambda = 2\pi/G = 2\pi/Q$ on the order of 20 to 70 nm for the materials listed in Tab. 1. Applying an electric field would rotate the orientation of the hexagonal magnetic grating around the field direction and allow to emit short-wavelength spin waves in different and tuneable directions transverse to \vec{H} . The continuous tunability of propagation directions has not yet been foreseen with conventional ferromagnets. By tilting the magnetic field \vec{H} stabilizing the SkL the grating coupler can be further adjusted and becomes versatile for even more spatial directions.

Applied electric or thermal currents have been shown to couple efficiently to a SkL. At very small electric current densities a SkL is depinned and shifted in space via spin-transfer torque (STT) [134, 135]. A magnon current, e.g., generated by a thermal gradient is also able to move skyrmions [136, 137, 138, 139, 140]. It has been also experimentally demonstrated that a thermal current might induce a continuous rotation of the SkL [141, 142]. Interestingly, micromagnetic simulations have suggested that a linearly polarized microwave field applied to a chiral magnet can displace both an individual skyrmion and a SkL in the presence of a symmetry-breaking magnetic field component. The maximum velocity is found for a frequency of the microwave that coincides with the resonance frequency of the breathing mode of the skyrmions [143]. These effects allow for the field- or current-controlled positioning of skyrmion-based magnonic crystals. In a moving SkL Doppler-shift like frequency variations of spin waves might be anticipated [144].

It is interesting to compare the magnon band structures found for hexagonal skyrmion lattices with the ones that were discussed for hexagonal lattices formed by bubble domains several decades ago. The dynamics of individual bubble domains and corresponding lattices was reviewed in Ref. [31]. We follow Ref. [31] and summarize the main aspects here. Bubble domains exist in epitaxial layers of ferrimagnetic garnets that are usually several micrometer thick and possess a perpendicular magnetic anisotropy but no or only a small DMI. Due to dipolar interaction, a periodic lattice of bubble domains is formed when a specific magnetic field is applied perpendicular to the film plane. If the distance between periodically arranged bubble domains is small, a magnonic crystal like band structure results from mainly magnetic dipole interactions. Allowed minibands can be classified in terms of two acoustic branches and one optical branch covering a frequency band of a few tens of megahertz for a 5 micrometer thick garnet. For the acoustic branches relatively large group velocities on the order of 100 m/s were expected in case of small edge-to-edge separations of bubble domains compared to their diameter. Already in 1979, the authors of Ref. [31] speculated that corresponding spin waves possessed potential as information signal carriers. Interestingly, bubble domain lattices allowed for reconfigurable magnon band structures [145]. However it was noted that the experimental realization of a lattice with identically hard bubbles appeared to be difficult [31]. In chiral magnets reviewed here, the pitch vector introduced by DMI enables the formation of regular periodic lattices with identical skyrmions.

4.2. Shape-, surface-, and orientation dependent effects

The resonance frequencies of the uniform $\pm Q$ modes of the conical helix strongly depend on the shape of the sample as illustrated in Fig. 8. For the breathing, CW and CCW modes of the skyrmion lattice the variation of eigenfrequencies with demagnetization factors is less pronounced [34]. Still the order of magnon bands in the skyrmion lattice varies with the strength of the effective dipolar interaction as shown for MnSi and Cu₂OSeO₃ in Fig. 11.

The interplay of bulk DMI and shape anisotropy leads to a linear polarization of the magnetization dynamics in the spin-helix state at small magnetic field, see section 3.2.2. Relevant eigenfrequencies are in the few GHz frequency regime for which transmission lines and coplanar waveguides are impedance matched and guide linearly-polarized microwaves efficiently on microchips. In conventional ferro- and ferrimagnets such linearly polarized spin-precessional motion is not accomplished. For

them the spin-precessional motion is elliptically or circularly polarized. Helical modes in chiral magnets with bulk DMI are linearly polarized at small fields and thus ideally couple to the linear polarization provided by the excitation fields of the conventional microwave technology [121].

The Dzyaloshinskii-Moriya interaction imposes also boundary conditions on the surface spins that result in a surface twist. In the FP phase, this leads to exchange spin waves that are localized to the surfaces of the sample [146, 147]. They will be further discussed below in section 4.6.1. In the SkL phase, surface spin-wave modes are also expected for a different reason. We have discussed in Fig. 11 that some of the magnon bands possess a non-trivial Chern number resulting from the non-trivial topology of the magnetic texture. According to the bulk-boundary correspondence, this implies the presence of topologically protected magnon edge states. Such magnon edge states have been previously discussed in a different context for the pyrochlore $\text{Lu}_2\text{V}_2\text{O}_7$ [148]. Moreover, the magnon bands with a finite Chern number should contribute to a magnon Hall effect, i.e., spin accumulation transverse to the magnon flow [141, 138, 139].

The three uniform excitation modes of the skyrmion lattice have been observed also for the Néel-type skyrmion lattice in the rhombohedral GaV_4S_8 [45, 46]. GaV_4S_8 hosts cycloidal spin structures and is characterized by a uniaxial anisotropy. Here, in the skyrmion lattice phase the breathing mode was experimentally found to possess a smaller resonance frequency than the CCW mode, i.e., the hierarchy of resonances differed from the one of the cubic chiral magnets in Fig. 13. This has also been theoretically confirmed by numerical simulations in Ref. [149]. Moreover, the eigenfrequencies and set of modes in this material class are expected to vary distinctly if an applied magnetic field is misaligned with respect to the easy axis. The misaligned field leads to a distortion of the skyrmion lattice with the concomitant change in resonance frequencies. In the cycloidal phase of GaV_4S_8 , two prominent modes were found that exhibited a large frequency splitting of several GHz. Here, the isotropic exchange and exchange anisotropy were argued to provide the energy scale attributed to the frequency splitting [45]. For the splitting of the two modes +Q and -Q in the helical modes of chiral magnets, the weaker dipolar interaction was relevant.

4.3. Magneto-chiral and multiferroic characteristics

The magnetoelectric coupling in Cu_2OSeO_3 imply that magnons exhibit both magnetic and electric activities which undergo interference effects and lead to directional dichroism. The relevant electric susceptibilities of the rotational and breathing modes in the SkL were reviewed in Ref. [84]. Linearly polarized microwaves guided through an SkL experience directional dichroism in both configurations for which the wavevector \vec{k}_{em} of the electromagnetic wave is either perpendicular or parallel to the magnetic field \vec{H} stabilizing the SkL. Counterpropagating electromagnetic waves encounter different absorption leading to nonreciprocal microwave properties (directional dichroism). For the case that \vec{k}_{em} is collinear with \vec{H} the directional dichroism is called magneto-chiral effect [84]. This effect has been found not only in the SkL of bulk Cu_2OSeO_3 but also in the conical and field-polarized phases. This kind of microwave nonreciprocity can thus be exploited over a broad frequency regime. For a detailed discussion we refer the reader to Refs. [88, 87]. To harvest such characteristics in microwave technology bulk materials with DMI are needed that are insulators and form skyrmions at room temperature. While bulk metals with

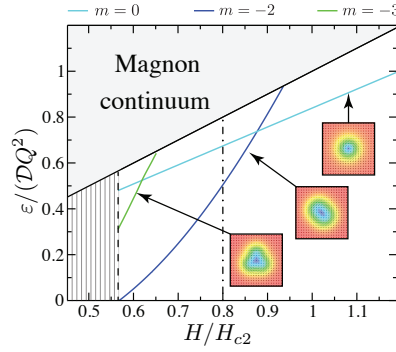


Figure 15. Magnon spectrum of the field-polarized state in the presence of a single skyrmion. There exist few magnon-skyrmion bound states below the magnon gap. The breathing mode parametrized by the angular momentum $m = 0$ extends up to high fields. A quadrupolar mode $m = -2$ appears for smaller fields whose resonance frequency vanishes for $H/H_{c2} \approx 0.56$ indicating the elliptical instability of the skyrmion [122]. A sextupolar mode $m = -3$ is only realized in a small magnetic field range above the elliptical instability. Taken from Ref. [139]

DMI and ultrathin metallic layers incorporating interfacial DMI provide magnetic skyrmions at room temperature [63, 73], to our knowledge, bulk insulators with room-temperature skyrmions have not yet been reported. Corresponding materials still need to be identified.

Finally, we remark that a direct electric field control of spin wave eigenfrequencies was also demonstrated in case of the cycloid spin structure of the room-temperature magnetoelectric material BiFeO_3 [150]. Here, the spin-wave frequency (> 600 GHz) was tuned electrically by over 30 %, in a non-volatile way and with virtually no power dissipation.

4.4. Magnonics with individual skyrmions

For skyrmion-based spin-electronics an individual skyrmion formed in a ferromagnetic matrix is expected to be technologically relevant [55]. In insulators, spin waves can then be used move the skyrmion, e.g., in a nanotrack [141, 138, 139, 151, 152, 153, 154]. For the functionalization of this magnon-skyrmion momentum-transfer, the understanding of the spin wave scattering off a skyrmion is essential.

When spin waves approach the skyrmion they scatter off it, and they can even form bound states. This magnon-skyrmion scattering problem was considered in Refs. [138, 139, 155] on the level of the exchange energy of Eq. (1). Here, we review the results of Ref. [139] where the magnon Hamiltonian was derived analytically and solved numerically for a finite in-plane magnon momentum $\vec{k}_\perp = (k_x, k_y, 0)$. The resulting spectrum (without uniaxial anisotropy) is shown in Fig. 15. Apart from scattering states above the magnon gap, there exist a few in-gap states corresponding to magnon-skyrmion bound modes. Above the critical field H_{c2} , there is only a single breathing mode for which the skyrmion radius oscillates in time. An additional quadrupolar and sextupolar mode appears only for smaller fields where the field-polarized state in a three-dimensional bulk material is already unstable. In the presence of a finite magnetic anisotropy, K , another mode with gyrotropic character might materialize below the magnon gap [156].

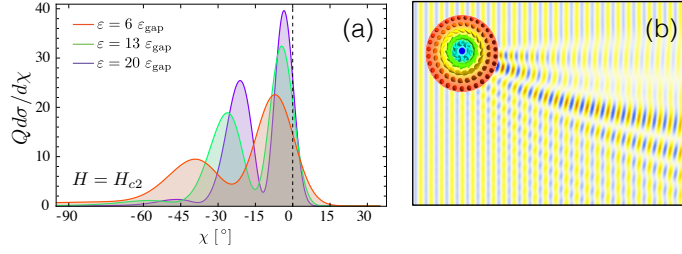


Figure 16. (a) Scattering cross section of a skyrmion at $H = H_{c2}$ as a function of in-plane polar angle χ for a monochromatic spin wave with three different energies ε . It is characterized by skew scattering and oscillations. (b) Stationary magnon wavefunction with $\varepsilon = 20\varepsilon_{\text{gap}}$ in the presence of a skyrmion indicating that spin waves are preferentially scattered to the right-hand side of the skyrmion. Without the skyrmion the spin wave would propagate horizontally from left to right. Taken from Ref. [139].

Only the breathing mode gives rise to an oscillating average magnetic dipole moment that can be excited with an ac magnetic field longitudinal to the dc field, i.e., along the z -axis. In the insulator Cu_2OSeO_3 the quadrupolar mode is accompanied with an oscillating electric dipole moment and could therefore be electrically excited (electromagnon) [139]. The breathing mode for Bloch-like skyrmions is also associated with an oscillating toroidal moment so that it can be excited also with a combination of in-plane magnetic and electric fields. In a magnetic layer, the conical state is suppressed and the field-polarized state remains stable below H_{c2} . The vertical dashed-dotted line in Fig. 15 then indicates a global instability where the energy of skyrmions becomes negative triggering the formation of a skyrmion crystal. Below this field, the skyrmion in the metastable field-polarized phase becomes elliptically unstable [122] when the resonance frequency of the quadrupolar mode vanishes.

The non-trivial topology of the skyrmion texture has a striking impact on the properties of the scattering states. Figure 16(a) shows the scattering cross section for magnons propagating in-plane with an energy that is large compared to the magnon gap: it is characterized by oscillations and strongly asymmetric with respect to forward scattering $\chi = 0$, i.e., there is skew scattering. This is also illustrated in panel (b) that shows a monochromatic magnon wave travelling from the left to the right hand side and scattering off a skyrmion. Both aspects can be transparently discussed by considering the magnon-skyrmion scattering problem in the high-energy limit [157]. In this limit, the magnon wave function ψ of Eq. (5) is simply governed by the Schrödinger equation

$$i\hbar\partial_t\psi = \left[\frac{(-i\hbar\vec{\nabla}_\perp - \vec{A}(\vec{r}))^2}{2m} + \varepsilon_{\text{gap}} \right] \psi \quad (37)$$

where, on the level of Eq. (1), the magnon gap ε_{gap} is proportional to the magnetic field, i.e., $\varepsilon_{\text{gap}} = g\mu_B\mu_0H$. The high-energy magnon propagating within the plane perpendicular to the field, $\vec{\nabla}_\perp = (\partial_x, \partial_y, 0)$, only scatters off a vector potential $\vec{A} = (A_x, A_y, 0)$. The associated flux density $\mathcal{B}_z = \partial_x A_y - \partial_y A_x$ is finite so that the magnon scatters off an emergent orbital magnetic field which is localized to the skyrmion area. This emergent orbital magnetic field arises from the non-trivial topology of the textured magnetization. When a high-energy magnon traverses the skyrmion texture, it locally adjusts its quantization axis to the spatially varying

magnetization. Mathematically, the geometric constraint imposed by the varying quantization axis leads to a spin connection which enters the Hamiltonian as a vector potential. Its total flux

$$\int dx dy \mathcal{B}_z = 4\pi\hbar \quad (38)$$

is quantized and related to the topological skyrmion charge of the soliton.

The magnon experiences an emergent Lorentz force due to \mathcal{B}_z that deflects its trajectory leading to the skew scattering. A finite density of skyrmions are thus expected to give rise to a topological magnon Hall effect [138]. For a given skyrmion configuration this Hall effect and the resulting spin accumulation might be used to read out a propagating spin wave signal. The oscillations in the scattering cross section of Fig. 16 (a) arise from a phenomenon known as rainbow scattering. The emergent field $\mathcal{B}_z = \mathcal{B}_z(\rho)$ only depends on the distance ρ to the skyrmion center. As a consequence, classical magnon trajectories with impact parameters $\pm b$, that pass the skyrmion at the same distance but either on its right- or left-hand side, will see the same flux and experience the same deflection angle. These trajectories interfere and lead to oscillations in the scattering cross section. The emergent orbital field \mathcal{B}_z for magnon excitations is characteristic for a topologically non-trivial magnetic texture. If the texture itself is moving with a finite velocity, an emergent electric field also arises according to Faraday's law [158]. This emergent electrodynamics is one of the exciting aspects of skyrmion textures, see Ref. [159] for a review.

An individual skyrmion might be stabilized dynamically in a ferromagnetic thin film by using a current-biased nanocontact providing STT locally [160]. On the one hand, such skyrmions could serve as scattering centers as discussed above. On the other hand, it was predicted that, in the presence of DMI, the breathing mode of the individual skyrmion can serve as an efficient and tuneable microwave signal generator [160].

4.5. Artificially tailored magnonic crystals based on skyrmions

The eigenmodes of an individual skyrmion within confined geometries like a disc were discussed in a series of theoretical works [161, 162, 163, 164]. In Ref. [165] Mruczkiewicz *et al.* investigated the spin-wave band structure arising from a periodic chain of nanodisks containing individual skyrmions. In Ref. [166], Ma *et al.* studied theoretically a long stripe in which a one-dimensional lattice of periodically ordered skyrmions were introduced dynamically via nanocontacts. In both cases, interfacial DMI and ultrathin films were considered. The skyrmions induced magnonic band structures with a dispersive character and collective properties [165, 166]. The stripe-based magnonic crystal has the advantage that both dipolarly and exchange-coupled modes can be controlled via the one-dimensional skyrmion lattice, while in chains of separated nanodisks only the dipolar coupling promotes propagating spin waves. Consequently, the work of Ma *et al.* addressed spin waves propagating along the channel with wavelengths down to about 50 nm, thereby entering the exchange dominated regime with spin-wave eigenfrequencies of several ten GHz [166]. In Ref. [165] in contrast, the allowed minibands with dispersive spin waves were near the original eigenfrequencies of the gyrotropic and breathing modes below 1 GHz and around 13 GHz, respectively. Group velocities were found to be small and only a few 10 m/s. These values reflect the small coupling between the skyrmion-containing

nanodisks. In Ref. [166], velocities are found to be an order of magnitude larger, offering a better signal transmission in a magnonic device.

4.6. Towards thin films with bulk DMI

Helimagnets incorporating bulk DMI have already been prepared via thin-film deposition techniques on different substrates. Typically, growth- and strain-induced anisotropies are found to modify the magnetic phase diagram with respect to the bulk material. In addition thin films often consist of domains in which the crystallites exhibit a different chirality. Preliminary measurements on the spin-wave damping in thin films of the helimagnet FeGe deposited by two different groups have provided damping parameters α that differ by almost two orders of magnitude [43, 162]. Here further research is needed to optimize chiral magnets in thin-film technology and exploit the full potential of bulk DMI. Propagating spin waves have been explored in the field-polarized phase of a thin platelet of Cu_2OSeO_3 that was extracted from a large single crystal using focused ion beam etching. When an in-plane field was parallel to the spin-wave wave vector a nonreciprocal spin-wave dispersion relation was extracted from the experimental spectra [110]. Cu_2OSeO_3 thus offers nonreciprocity of both transmitted electromagnetic waves and spin waves. A bulk sample of noncentrosymmetric LiFe_5O_8 (space group P4_132) with DMI was reported to exhibit a nonreciprocal spin-wave dispersion relation as well [167].

Before we discuss interesting properties that theory predicts for thin films with bulk DMI we comment on the role of thin films that host skyrmions due to interfacial DMI. Spin dynamics in metallic magnetic multilayers exhibiting relevant interfacial DMI has been explored both theoretically and experimentally. Theoretically it has been shown that such layers form narrow domain walls that channel or scatter spin waves [168, 169]. In the saturated magnetic state the interfacial DMI has been predicted to induce nonreciprocal spin-wave dispersion relations [170] that can be tailored via different multilayer compositions. Inelastic scattering of both electrons and light has been applied to such materials systems and showed spin-wave spectra exhibiting different eigenfrequencies for opposing wave-vector directions consistent with theoretical considerations [171, 172, 173]. Interfacial DMI thus enriches a magnonics-related thin-film technology beyond skyrmions [174]. For instance, nanomagnonic waveguides with unidirectional spin-wave propagation become possible [175]. However, metallic magnetic layers with DMI are expected to exhibit a broad linewidth [176], i.e., an increased damping of spin waves. We note that the microscopic mechanism behind interfacial DMI lies in spin-orbit coupling. In metallic ferromagnets, spin-orbit coupling leads to spin-wave damping due to precession-induced intra- and interband excitations of conduction electrons and subsequent electron scattering [177]. At the same time, metallic multilayers with non-collinear spin structures might experience enhanced spin-wave damping via spin pumping [81, 178, 179]. We suppose damping parameters α of metallic thin films hosting magnetic skyrmions to be four to five orders of magnitude worse compared to YIG which is the prototypical magnetic material in microwave technologies exploiting spin-precessional motion. When aiming at low spin-wave damping we suggest to focus on thin-film materials where an insulating magnet carries the spin waves. In insulating magnets, excitations of conduction electrons are not relevant and spin-wave damping is potentially small.

4.6.1. Spin waves in thin films: field-polarized and magnetic helix state We now turn to the theoretical discussion of the spin-wave spectrum in a film of a cubic chiral magnet described by Eqs. (1) and (3). The film is assumed to possess a thickness d that is comparable to an intrinsic length scale of the system, in particular, the pitch length $2\pi/Q$ (Tab. 1). In the following we further assume an infinitely large film whose normal is oriented along the z -axis. For the thin film, one might take into account an additional magnetic anisotropy in the free energy functional $F_{\text{aniso}} = \int d\vec{r} \mathcal{F}_{\text{aniso}}$ with

$$\mathcal{F}_{\text{aniso}} = K \hat{n}_z^2 \quad (39)$$

and anisotropy constant K . It corresponds to an easy-plane anisotropy for $K > 0$ and an easy-axis anisotropy for $K < 0$.

Large out-of-plane field: field-polarized state

The situation in thin films is generally complicated due to the boundary conditions of Eq. (4) that the magnetization must obey at the surfaces of the film. It is still tractable for a magnetic field applied along the film normal, i.e., along the z -axis, $\vec{H} = H \hat{z}$. In this case the magnetization is fully polarized at large fields and $\hat{n}_{\text{eq}} = \hat{z}$. As the film is infinite and translationally invariant, we can perform a partial Fourier transform and consider the magnon wavefunction $\vec{\Psi}_{\vec{k}_\perp, \omega}(z)$ as a function of in-plane momentum $\vec{k}_\perp = (k_x, k_y, 0)$, frequency ω , and the spatial z coordinate. The stationary wave equation can be cast into the form

$$\hbar\omega\tau^z \vec{\Psi}_{\vec{k}_\perp, \omega}(z) = \mathcal{H}_{\text{loc}} \vec{\Psi}_{\vec{k}_\perp, \omega}(z) + \int_0^d dz' \mathcal{K}(\vec{k}_\perp, z - z') \vec{\Psi}_{\vec{k}_\perp, \omega}(z') \quad (40)$$

for a film located within the interval $z \in [0, d]$. The local part of the Hamiltonian reads

$$\mathcal{H}_{\text{loc}} = \mathcal{D}(-1\partial_z^2 - i2Q\tau^z\partial_z) + (\mathcal{D}k_\perp^2 + g\mu_B\mu_0 H_{\text{int}} - \frac{g\mu_B 2K}{M_s})1 \quad (41)$$

with the internal field $H_{\text{int}} = H - M_s$ corresponding to a demagnetization factor $N_z = 1$. The nonlocal part derives from the dipolar interaction and its kernel is given by

$$\mathcal{K}(\vec{k}_\perp, z) = \frac{g\mu_B\mu_0 M_s}{4|\vec{k}_\perp|} e^{-|\vec{k}_\perp||z|} \begin{pmatrix} k_+ k_- & k_-^2 \\ k_+^2 & k_+ k_- \end{pmatrix} \quad (42)$$

in the same notation as in Eq. (10). Importantly, on the two surfaces of the film, $z = 0$ and $z = d$, the wavefunction must obey the boundary conditions that follow from Eq. (4). In the absence of surface pinning, they are given by

$$(-i\partial_z + Q\tau^z) \vec{\Psi}_{\vec{k}_\perp, \omega}(z) \Big|_{\text{surface}} = 0. \quad (43)$$

For zero in-plane momentum $\vec{k}_\perp = 0$ the non-local part vanishes, $\mathcal{K}(\mathbf{0}, z) = 0$, and the eigenvalue problem becomes local. The eigenfunctions obeying the above boundary conditions are then readily obtained

$$\vec{\Psi}_{\sigma, p}(z) = \frac{1}{N_p} \cos\left(\frac{\pi p}{d} z\right) e^{-iQ\tau^z z} \begin{pmatrix} 1 + \sigma \\ 1 - \sigma \end{pmatrix} \quad (44)$$

with $\sigma = \pm 1$ and a normalization constant N_p . These eigenfunctions describe the so-called perpendicular standing spin-wave (PSSW) modes of the film [180] in the

presence of DMI specified by the discrete quantum number $p = 0, 1, 2, 3, \dots$. The corresponding eigenfrequencies are $\omega_{\pm,p} = \pm\omega_p$ with

$$\hbar\omega_p = \mathcal{D} \left(\frac{\pi p}{d} \right)^2 + g\mu_B\mu_0(H - H_{c2,z}). \quad (45)$$

We introduced the critical field $H_{c2,z} = M_s + \frac{2K}{\mu_0 M_s} + \frac{\mathcal{D}Q^2}{9\mu_B\mu_0}$ that is assumed to be positive.

The spectrum given by Eq. (45) differs from that of a field-polarized ferromagnetic film. The mode $p = 0$ does not correspond to the uniform mode but carries a finite wavevector. For decreasing H , its gap vanishes at the critical field $H_{c2,z}$ triggering the formation of the helical state. The boundary conditions of Eq. (43) result in the additional oscillating factor e^{-iQz} (for $\sigma = 1$). It was pointed out in Ref. [181] that the eigenfunction given by Eq. (44) corresponds to the superposition of two non-reciprocal spin waves with wavevectors $\frac{\pi p}{d} + Q$ and $-\frac{\pi p}{d} + Q$. Importantly, the dynamic correction to the uniform magnetization is proportional to the integral $\int_0^d dz \bar{\Psi}_{+,p}(z)$ that is finite for all quantum numbers p due to the additional phase factor e^{-iQz} . As a result, all PSSW modes couple to a uniform oscillating magnetic field [181]. This is in contrast to a ferromagnetic film for which only the Kittel mode is excited by a uniform oscillating field if spins were free at the surfaces.

In the presence of a finite in-plane momentum \vec{k}_\perp the nonlocal part \mathcal{K} of the wave equation (40) must be considered. This is usually done either approximately or numerically, and, for ferromagnets, it gives rise to the magnetostatic forward volume mode (MSFVM). Recent microwave absorption experiments on films of FeGe for an applied out-of-plane field have found two resonances at high fields that were interpreted as PSSW modes [43].

Large in-plane field: twisted surface spins

For a large magnetic field within the plane of the film, say, along the x -axis, the magnetization is not completely polarized and $\hat{n}_{\text{eq}} \neq \hat{x}$. It is twisted close to the film surfaces due to the boundary conditions given by Eq. (4), and this boundary twist was experimentally investigated, e.g., in a film of MnSi [108] as well as in nanowires and lamellae of FeGe [182, 183]. The influence of this twist on the magnon spectrum was addressed theoretically in Refs. [146, 147] neglecting however dipolar interactions. It was found that the twist acts as an attractive potential for the exchange spin waves resulting in modes localized to the two surfaces. The mechanism for localization is thus different from surface- and edge confined magnetostatic modes already explored in magnonics, i.e., Damon-Eshbach modes [184] and modes in spin-wave wells [185], respectively. Intriguingly, a recent theoretical work predicts that in the presence of a surface twist and corresponding edge magnons a specific field protocol can be implemented to create a chain of skyrmions at the edge of a field-polarized two-dimensional chiral magnet [147]. Omitting the surface twist, Ref. [170] theoretically discussed the full dipole-exchange spin-wave spectrum. A numerical micromagnetic simulation of the magnon spectrum in this configuration was recently presented in Ref. [186] together with a comparison to microwave absorption experiments on FeGe films. Measurements in this geometry have been also performed on Cu_2OSeO_3 [110].

Thin film with spin-helix state

We now turn to a discussion of spin-wave properties in the spin helix state. The treatment for a general orientation of the magnetic field is again complicated by the boundary conditions of Eq. (4). Only for a magnetic field aligned along the film normal (z -axis), the conical helix of Eq. (15) automatically fulfils the boundary conditions of Eq. (4). We restrict our discussion to the case of vanishing in-plane magnon momentum $\vec{k}_\perp = 0$. Following similar steps as in the context of Eq. (45), the eigenfrequencies of the PSSW modes are found to read

$$\hbar\omega_p = \sqrt{\mathcal{D}} \frac{\pi p}{d} \sqrt{\mathcal{D} \left(\frac{\pi p}{d}\right)^2 + g\mu_B\mu_0 H_{c2,z} \left(1 - \left(\frac{H}{H_{c2,z}}\right)^2\right)}. \quad (46)$$

with $p = 0, 1, 2, \dots$ and the critical field $H_{c2,z} = M_s + \frac{2K}{\mu_0 M_s} + \frac{\mathcal{D}Q^2}{g\mu_B\mu_0} > 0$. This formula is valid for $H \leq H_{c2,z}$. At the critical field $H_{c2,z}$ the eigenfrequencies of Eq. (46) directly connect to Eq. (45) for each p smoothly.

For a magnetic field within the plane of the film, different regimes might be realized. For strong easy-plane anisotropy [§], the helix axis might remain aligned along the film normal. Similar to monoaxial chiral magnets [187], the in-plane field then distorts the helix to a chiral soliton lattice, which has been recently observed in films of FeGe [188]. The resonances of the chiral soliton lattice have been studied theoretically in Ref. [189]. In the other limit of easy-axis anisotropy, the helix axis rotates into the film plane, and the boundary conditions (4) result in a deformation of the helix close to the surfaces. Even more complicated situations arise for weak or canted magnetic fields.

5. Concluding remarks

We reviewed the collective spin excitations in chiral magnets hosting the skyrmion lattice phase. We discussed how noncollinear spin structures such as spin helices and skyrmions enrich the dynamic properties of magnetic materials. We argued that beyond spintronics also magnonics is expected to benefit from developments in skyrmionics. One can anticipate for instance nonreciprocal microwave components, magnonic crystals and grating couplers controlled by magnetic and electric fields, nanoscale microwave generators, and Hall effect readout of spin-wave signals. Bulk chiral magnets with small damping open novel perspectives for the control and manipulation of both spin waves and electromagnetic waves in solids.

Acknowledgements

M.G. acknowledges support from the Deutsche Forschungsgemeinschaft (DFG) via SFB 1143 "Correlated Magnetism: From Frustration to Topology" and grant GA 1072/5-1. D.G. acknowledges support by the DFG via the Transregio TRR80 "From electronic correlations to functionality". The Swiss National Science Foundation (SNSF) funds magnonics research on skyrmion-hosting materials via the sinergia network "Nanoskyrmionics" (grant CRSII5-171003).

§ The effective anisotropy is determined here by the combination of the explicit anisotropy K and the dipolar interaction, and it is quantified by $K_{\text{eff}} = K + \mu_0 M_s^2/2$

Appendix A. Dipolar matrix elements

Here, we present the matrix elements $\mathcal{H}_{\text{dip}}^{\alpha\beta}(\vec{k})$ entering the spin wave equation of Eq. (17). We will use the matrix representation

$$\mathcal{H}_{\text{dip}}(\vec{k}) = \begin{pmatrix} \mathcal{H}_{\text{dip}}^{1,1}(\vec{k}) & \mathcal{H}_{\text{dip}}^{1,0}(\vec{k}) & \mathcal{H}_{\text{dip}}^{1,-1}(\vec{k}) \\ \mathcal{H}_{\text{dip}}^{0,1}(\vec{k}) & \mathcal{H}_{\text{dip}}^{0,0}(\vec{k}) & \mathcal{H}_{\text{dip}}^{0,-1}(\vec{k}) \\ \mathcal{H}_{\text{dip}}^{-1,1}(\vec{k}) & \mathcal{H}_{\text{dip}}^{-1,0}(\vec{k}) & \mathcal{H}_{\text{dip}}^{-1,-1}(\vec{k}) \end{pmatrix}. \quad (\text{A.1})$$

For zero wavevectors, $\vec{k} = 0$, the matrix elements depend on the demagnetization factors N_x , N_y and N_z ,

$$\mathcal{H}_{\text{dip}}(\vec{0}) = \frac{\mathcal{D}Q^2\lambda_{\text{con}}^{\text{int}}}{2} \begin{pmatrix} \frac{N_x+N_y}{2} \left(\frac{1+c^2}{2} + \frac{s^2}{2} \tau^x + c\tau^z \right) & 0 & \frac{N_x-N_y}{2} \left(-\frac{s^2}{2} - ic\tau^y - \frac{1+c^2}{2} \tau^x \right) \\ 0 & N_z s^2 (1-\tau^x) & 0 \\ \frac{N_x-N_y}{2} \left(-\frac{s^2}{2} + ic\tau^y - \frac{1+c^2}{2} \tau^x \right) & 0 & \frac{N_x+N_y}{2} \left(\frac{1+c^2}{2} + \frac{s^2}{2} \tau^x - c\tau^z \right) \end{pmatrix}, \quad (\text{A.2})$$

where we abbreviated $s = \sin \theta$ and $c = \cos \theta$.

For wavevectors, $|\vec{k}| \gg 1/L$, large compared to the inverse linear size of the sample L , the matrix elements are given by

$$\mathcal{H}_{\text{dip}}(\vec{k}) = \frac{\mathcal{D}Q^2\lambda_{\text{con}}^{\text{int}}}{4} \begin{pmatrix} k_- k_+ \left(\frac{1+c^2}{2} + \frac{s^2}{2} \tau^x + c\tau^z \right) & k_- k_z \left(-cs(1-\tau^x) + is(\tau^y + i\tau^z) \right) & k_- k_- \left(-\frac{s^2}{2} - ic\tau^y - \frac{1+c^2}{2} \tau^x \right) \\ k_z k_+ \left(-cs(1-\tau^x) - is(\tau^y - i\tau^z) \right) & 2k_z k_z s^2 (1-\tau^x) & k_z k_- \left(-cs(1-\tau^x) + is(\tau^y - i\tau^z) \right) \\ k_+ k_+ \left(-\frac{s^2}{2} + ic\tau^y - \frac{1+c^2}{2} \tau^x \right) & k_+ k_z \left(-cs(1-\tau^x) - is(\tau^y + i\tau^z) \right) & k_+ k_- \left(\frac{1+c^2}{2} + \frac{s^2}{2} \tau^x - c\tau^z \right) \end{pmatrix} \quad (\text{A.3})$$

where we used $k_{\pm} = k_x \pm ik_y$. Note, that only the center element remains finite for $\vec{k} \parallel \hat{z} \parallel \vec{Q}$, particularly if $\vec{k} = n\vec{Q}$ for $n \in \mathbb{Z}$ and $n \neq 0$.

References

- [1] Portnichenko P Y, Romhanyi J, Onykienko Y A, Henschel A, Schmidt M, Cameron A S, Surmach M A, Lim J A, Park J T, Schneidewind A, Abernathy D L, Rosner H, van den Brink J and Inosov D S 2016 *Nat. Commun.* **7** 10725 article URL <http://dx.doi.org/10.1038/ncomms10725>
- [2] Néel L 1970 *Nobel lecture*
- [3] Meiklejohn W H and Bean C P 1956 *Phys. Rev.* **102**(5) 1413–1414 URL <http://link.aps.org/doi/10.1103/PhysRev.102.1413>
- [4] Gurevich A G and Melkov G A 1996 *Magnetization Oscillations and Waves* (Boca Raton: CRC Press)
- [5] Nikitov S A, Kalyabin D V, Lisenkov I V, Slavin A, Barabanenkov Y N, Osokin S A, Sadovnikov A V, Beginin E N, Morozova M A, Filimonov Y A, Khivintsev Y V, Vysotsky S L, Sakharov V K and Pavlov E S 2015 *Physics-Uspokhi* **58** 1002 URL <http://stacks.iop.org/1063-7869/58/i=10/a=1002>
- [6] Sparks M 1964 *Ferromagnetic-Relaxation Theory* (McGraw-Hill)
- [7] Klingler S, Maier-Flaig H, Dubs C, Surzhenko O, Gross R, Huebl H, Goennenwein S T B and Weiler M 2017 *Appl. Phys. Lett.* **110** 092409 (Preprint <http://dx.doi.org/10.1063/1.4977423>) URL <http://dx.doi.org/10.1063/1.4977423>
- [8] Schoen M A W, Thonig D, Schneider M L, Silva T J, Nembach H T, Eriksson O, Karis O and Shaw J M 2016 *Nat. Phys.* **12** 839–842
- [9] Serga A, Chumak A and Hillebrands B 2010 *J. Phys. D: Appl. Phys.* **43** 264002
- [10] Yu H, d'Allivy Kelly O, Cros V, Bernard R, Bortolotti P, Anane A, Brandl F, Huber R, Stasinopoulos I and Grundler D 2014 *Sci. Rep.* **4** 6848
- [11] Yu H, d'Allivy Kelly O, Cros V, Bernard R, Bortolotti P, Anane A, Brandl F, Heimbach F and Grundler D 2016 *Nat. Commun.* **7** 11255
- [12] Kruglyak V V, Demokritov S O and Grundler D 2010 *J. Phys. D: Appl. Phys.* **43** 264001 URL <http://stacks.iop.org/0022-3727/43/i=26/a=264001>
- [13] Lenk B, Ulrichs H, Garbs F and Müntzenberg M 2011 *Phys. Rep.* **507** 107 – 136 ISSN 0370-1573 URL <http://www.sciencedirect.com/science/article/pii/S0370157311001694>

- [14] Chumak A V, Vasyuchka V I, Serga A A and Hillebrands B 2015 *Nat. Phys.* **11** 453
- [15] Stamps R L, Breitzkreutz S, Kerman J, Chumak A V, Otani Y, Bauer G E W, Thiele J U, Bowen M, Majetich S A, Klui M, Prejbeanu I L, Dieny B, Dempsey N M and Hillebrands B 2014 *J. Phys. D: Appl. Phys.* **47** 333001 URL <http://stacks.iop.org/0022-3727/47/i=33/a=333001>
- [16] 2015 *International Technology Roadmap for Semiconductors* (Semiconductor Industry Association)
- [17] Khitun A, Bao M and Wang K L 2010 *J. Phys. D: Appl. Phys.* **43** 264005 URL <http://stacks.iop.org/0022-3727/43/i=26/a=264005>
- [18] Gertz F, Kozhevnikov A, Filimonov Y and Khitun A 2015 *IEEE Tran. Magn.* **51** 1 ISSN 0018-9464
- [19] Wang Z K, Zhang V L, Lim H S, Ng S C, Kuok M H, Jain S and Adeyeye A O 2010 *ACS Nano* **4** 643–648 pMID: 20099868 (*Preprint* <http://dx.doi.org/10.1021/nn901171u>) URL <http://dx.doi.org/10.1021/nn901171u>
- [20] Tacchi S, Duerr G, Klos J W, Madami M, Neusser S, Gubbiotti G, Carlotti G, Krawczyk M and Grundler D 2012 *Phys. Rev. Lett.* **109**(13) 137202 URL <http://link.aps.org/doi/10.1103/PhysRevLett.109.137202>
- [21] Krawczyk M, Mamica S, Mruczkiewicz M, Klos J W, Tacchi S, Madami M, Gubbiotti G, Duerr G and Grundler D 2013 *J. Phys. D: Appl. Phys.* **46** 495003 URL <http://stacks.iop.org/0022-3727/46/i=49/a=495003>
- [22] Krawczyk M and Grundler D 2014 *J. Phys.: Condens. Matter* **26** 123202 URL <http://stacks.iop.org/0953-8984/26/i=12/a=123202>
- [23] Topp J, Heitmann D, Kostylev M P and Grundler D 2010 *Phys. Rev. Lett.* **104**(20) 207205 URL <http://link.aps.org/doi/10.1103/PhysRevLett.104.207205>
- [24] Tacchi S, Madami M, Gubbiotti G, Carlotti G, Goolaup S, Adeyeye A O, Singh N and Kostylev M P 2010 *Phys. Rev. B* **82**(18) 184408 URL <http://link.aps.org/doi/10.1103/PhysRevB.82.184408>
- [25] Arabinda Haldar D K and Adeyeye A O 2016 *Nat. Nano.* **11** 437–443
- [26] Chumak A V, Tiberkevich V S, Karenowska A, Serga A, Gregg J, Slavin A N and Hillebrands B 2010 *Nat. Commun.* **1** 141 article URL <http://dx.doi.org/10.1038/ncomms1142>
- [27] Vogel M, Chumak A V, Waller E H, Langner T, Vasyuchka V I, Hillebrands B and von Freymann G 2015 *Nat. Phys.* **11** 487–491 ISSN 1745-2473 letter URL <http://dx.doi.org/10.1038/nphys3325>
- [28] Albisetti E, Petti D, Pancaldi M, Madami M, Tacchi S, Curtis J, P King W, Papp A, Csaba G, Porod W, Vavassori P, Riedo E and Bertacco R 2016 *Nat. Nano.* **11** 545–551 ISSN 1748-3387 article URL <http://dx.doi.org/10.1038/nnano.2016.25>
- [29] Brandl F, Franke K, Lahtinen T, van Dijken S and Grundler D 2014 *Sol. St. Commun.* **198** 13–17 ISSN 0038-1098 sI: Spin Mechanics URL <http://www.sciencedirect.com/science/article/pii/S0038109813005966>
- [30] Duerr G, Huber R and Grundler D 2012 *J. Phys.: Condens. Matter* **24** 024218 URL <http://stacks.iop.org/0953-8984/24/i=2/a=024218>
- [31] Malozemoff A P and Slonczewski J C 1979 *Magnetic domain walls in bubble materials* (*Advances Solid State Science* vol Supplement 1) (New York: Academic Press) ISBN 0-12-002951-0
- [32] Bak P and Jensen M H 1980 *J. Phys. C: Solid State* **13** L881 URL <http://stacks.iop.org/0022-3719/13/i=31/a=002>
- [33] Seki S, Yu X Z, Ishiwata S and Tokura Y 2012 *Science* **336** 198 URL <http://www.sciencemag.org/content/336/6078/198.full.html>
- [34] Schwarze T, Waizner J, Garst M, Bauer A, Stasinopoulos I, Berger H, Pfeiderer C and Grundler D 2015 *Nat. Mater.* **14** 478–483 URL <http://dx.doi.org/10.1038/nmat4223>
- [35] Date M, Okuda K and Kadowaki K 1977 *J. Phys. Soc. Jap.* **42** 1555
- [36] Janoschek M, Bernlochner F, Dunsiger S, Pfeiderer C, Böni P, Roessli B, Link P and Rosch A 2010 *Phys. Rev. B* **81**(21) 214436 URL <http://link.aps.org/doi/10.1103/PhysRevB.81.214436>
- [37] Kugler M, Brandl G, Waizner J, Janoschek M, Georgii R, Bauer A, Seemann K, Rosch A, Pfeiderer C, Böni P and Garst M 2015 *Phys. Rev. Lett.* **115**(9) 097203 URL <http://link.aps.org/doi/10.1103/PhysRevLett.115.097203>
- [38] Onose Y, Okamura Y, Seki S, Ishiwata S and Tokura Y 2012 *Phys. Rev. Lett.* **109** 037603 URL <http://link.aps.org/doi/10.1103/PhysRevLett.109.037603>
- [39] Okamura Y, Kagawa F, Mochizuki M, Kubota M, Seki S, Ishiwata S, Kawasaki M, Onose Y and Tokura Y 2013 *Nat. Commun.* **4** 2391 URL <http://www.nature.com/ncomms/2013/>

- 130830/ncomms3391/full/ncomms3391.html
- [40] Tucker G S, White J S, Romhányi J, Szaller D, Kézsmárki I, Roessli B, Stuhr U, Magrez A, Groitl F, Babkevich P, Huang P, Živković I and Rønnow H M 2016 *Phys. Rev. B* **93**(5) 054401 URL <http://link.aps.org/doi/10.1103/PhysRevB.93.054401>
- [41] Watanabe H, Tazuke Y and Nakajima H 1985 *J. Phys. Soc. Jap.* **54** 3978
- [42] Haraldson S, Pettersson L and Bhagat S 1978 *Journal of Magnetic Resonance (1969)* **32** 115 – 120 ISSN 0022-2364 URL <http://www.sciencedirect.com/science/article/pii/0022236478900811>
- [43] Zhang S L, Stasinopoulos I, Lancaster T, Xiao F, Bauer A, Rucker F, Baker A A, Figueroa A I, Salman Z, Pratt F L, Blundell S J, Prokscha T, Suter A, Waizner J, Garst M, Grundler D, van der Laan G, Pfeleiderer C and Hesjedal T 2017 *Scientific Reports* **7** 123 ISSN 2045-2322 URL <http://dx.doi.org/10.1038/s41598-017-00201-z>
- [44] Siegfried S A, Sukhanov A S, Altyntbaev E V, Honecker D, Heinemann A, Tsvyashchenko A V and Grigoriev S V 2017 *Phys. Rev. B* **95**(13) 134415 URL <https://link.aps.org/doi/10.1103/PhysRevB.95.134415>
- [45] Ehlers D, Stasinopoulos I, Tsurkan V, Krug von Nidda H A, Fehér T, Leonov A, Kézsmárki I, Grundler D and Loidl A 2016 *Phys. Rev. B* **94**(1) 014406 URL <http://link.aps.org/doi/10.1103/PhysRevB.94.014406>
- [46] Ehlers D, Stasinopoulos I, Kzsmrki I, Fehr T, Tsurkan V, von Nidda H A K, Grundler D and Loidl A 2017 *J. Phys.: Condens. Matter* **29** 065803 URL <http://stacks.iop.org/0953-8984/29/i=6/a=065803>
- [47] Bauer A and Pfeleiderer C 2016 *Generic Aspects of Skyrmion Lattices in Chiral Magnets* (Cham: Springer International Publishing) pp 1–28 ISBN 978-3-319-25301-5
- [48] Nagaosa N and Tokura Y 2013 *Nat. Nanotech.* **8** 899
- [49] Garst M 2016 *Topological Skyrmion Dynamics in Chiral Magnets* (Cham: Springer International Publishing) pp 29–53 ISBN 978-3-319-25301-5
- [50] Mühlbauer S, Binz B, Jonietz F, Pfeleiderer C, Rosch A, Neubauer A, Georgii R and Böni P 2009 *Science* **323** 915 URL <http://www.sciencemag.org/content/323/5916/915.full>
- [51] Pfeleiderer C, Adams T, Bauer A, Biberacher W, Binz B, Birkelbach F, Bni P, Franz C, Georgii R, Janoschek M, Jonietz F, Keller T, Ritz R, Mhlbauer S, Mnzer W, Neubauer A, Pedersen B and Rosch A 2010 *J. Phys.: Condens. Matter* **22** 164207 URL <http://stacks.iop.org/0953-8984/22/i=16/a=164207>
- [52] Yu X Z, Onose Y, Kanazawa N, Park J H, Han J H, Matsui Y, Nagaosa N and Tokura Y 2010 *Nature* **465** 901 URL <http://www.nature.com/nature/journal/v465/n7300/full/nature09124.html>
- [53] Hirohata A and Takanashi K 2014 *J. Phys. D: Appl. Phys.* **47** 193001 URL <http://stacks.iop.org/0022-3727/47/i=19/a=193001>
- [54] Fert A, Cros V and Sampaio J 2013 *Nat. Nano.* **8** 152 URL <http://www.nature.com/nnano/journal/v8/n3/full/nnano.2013.29.html>
- [55] Sampaio J, Cros V, Rohart S, Thiaville A and Fert A 2013 *Nat. Nano.* **8** 839–844 URL <http://dx.doi.org/10.1038/nnano.2013.210>
- [56] Iwasaki J, Mochizuki M and Nagaosa N 2013 *Nat. Nano.* **8** 742 URL <http://www.nature.com/nnano/journal/v8/n10/full/nnano.2013.176.html>
- [57] Zhang X, Ezawa M and Zhou Y 2015 *Sci. Rep.* **5** URL <http://dx.doi.org/10.1038/srep09400>
- [58] Zhang S, Wang J, Zheng Q, Zhu Q, Liu X, Chen S, Jin C, Liu Q, Jia C and Xue D 2015 *New J. Phys.* **17** 023061 URL <http://stacks.iop.org/1367-2630/17/i=2/a=023061>
- [59] Kang W, Huang Y, Zhang X, Zhou Y and Zhao W 2016 *Proceedings of the IEEE* **104** 2040–2061 ISSN 0018-9219
- [60] Finocchio G, Büttner F, Tomasello R, Carpentieri M and Kläui M 2016 *J. Phys. D: Appl. Phys.* **49** 423001 URL <http://stacks.iop.org/0022-3727/49/i=42/a=423001>
- [61] Heinze S, von Bergmann K, Menzel M, Brede J, Kubetzka A, Wiesendanger R, Bihlmayer G and Blugel S 2011 *Nat. Phys.* **7** 713–718 ISSN 1745-2473 URL <http://dx.doi.org/10.1038/nphys2045>
- [62] Romming N, Hanneken C, Menzel M, Bickel J E, Wolter B, von Bergmann K, Kubetzka A and Wiesendanger R 2013 *Science* **341** 636–639 ISSN 0036-8075 (Preprint <http://science.sciencemag.org/content/341/6146/636.full.pdf>) URL <http://science.sciencemag.org/content/341/6146/636>
- [63] Soumyanarayanan A, Reyren N, Fert A and Panagopoulos C 2016 *Nature* **539** 509–517
- [64] Jiang W *et al* 2015 *Science* **349** 283–286
- [65] Moreau-Luchaire C *et al* 2016 *Nat. Nanotechn.* **11** 444–448
- [66] Boulle O *et al* 2016 *Nat. Nanotechn.* **11** 449–454

- [67] Woo S, Litzius K, Kruger B, Im M Y, Caretta L, Richter K, Mann M, Krone A, Reeve R M, Weigand M, Agrawal P, Lemesh I, Mawass M A, Fischer P, Klaui M and Beach G S D 2016 *Nat. Mater.* **15** 501–506 ISSN 1476-1122 letter URL <http://dx.doi.org/10.1038/nmat4593>
- [68] Gilbert D A, Maranville B B, Balk A L, Kirby B J, Fischer P, Pierce D T, Unguris J, Borchers J A and Liu K 2015 *Nat. Commun.* **6** 8462
- [69] Rayleigh L 1887 *Phil. Mag.* **24** 145–159
- [70] Baba T 2008 *Nat. Photonics* **2** 465–473
- [71] Bogdanov A N and Röbber U K 2001 *Phys. Rev. Lett.* **87**(3) 037203 URL <https://link.aps.org/doi/10.1103/PhysRevLett.87.037203>
- [72] Koralek J D, Meier D, Hinton J P, Bauer A, Parameswaran S A, Vishwanath A, Ramesh R, Schoenlein R W, Pfeiderer C and Orenstein J 2012 *Phys. Rev. Lett.* **109**(24) 247204 URL <http://link.aps.org/doi/10.1103/PhysRevLett.109.247204>
- [73] Tokunaga Y, Yu X Z, White J S, Ronnow H M, Morikawa D, Taguchi Y and Tokura Y 2015 *Nat. Commun.* **6** URL <http://dx.doi.org/10.1038/ncomms8638>
- [74] Kobets M I, Dergachev K G, Khatsko E N, Rykova A I, Lemmens P, Wulferding D and Berger H 2010 *Low Temp. Phys.* **36** 176–179 URL <http://scitation.aip.org/content/aip/journal/ltp/36/2/10.1063/1.3319505>
- [75] Belesi M, Rousochatzakis I, Wu H C, Berger H, Shvets I V, Mila F and Ansermet J P 2010 *Phys. Rev. B* **82** 094422 URL <http://link.aps.org/doi/10.1103/PhysRevB.82.094422>
- [76] Seki S, Ishiwata S and Tokura Y 2012 *Phys. Rev. B* **86** 060403 URL <http://link.aps.org/doi/10.1103/PhysRevB.86.060403>
- [77] Maisuradze A, Shengelaya A, Berger H, Djokić D M and Keller H 2012 *Phys. Rev. Lett.* **108**(24) 247211 URL <http://link.aps.org/doi/10.1103/PhysRevLett.108.247211>
- [78] Levatić I, Šurića V, Berger H and Živković I 2014 *Phys. Rev. B* **90**(22) 224412 URL <http://link.aps.org/doi/10.1103/PhysRevB.90.224412>
- [79] White J S, Levatić I, Omrani A A, Egetenmeyer N, Prša K, Živković I, Gavilano J L, Kohlbrecher J, Bartkowiak M, Berger H and Rønnow H M 2012 *J. Phys.: Condens. Matter* **24** 432201 URL <http://stacks.iop.org/0953-8984/24/i=43/a=432201>
- [80] Ogawa N, Seki S and Tokura Y 2015 *Sci. Rep.* **5** 9552 URL <http://www.nature.com/srep/2015/150330/srep09494/full/srep09552.html>
- [81] Hirobe D, Shiomi Y, Shimada Y, Ohe J and Saitoh E 2015 *J. Appl. Phys.* **117** 053904 URL <http://scitation.aip.org/content/aip/journal/jap/117/5/10.1063/1.4907040>
- [82] Ruff E, Lunkenheimer P, Loidl A, Berger H and Krohns S 2015 *Sci. Rep.* **5** 15025
- [83] Zhang S L, Bauer A, Burn D M, Milde P, Neuber E, Eng L M, Berger H, Pfeiderer C, van der Laan G and Hesjedal T 2016 *Nano Letters* **16** 3285–3291 pMID: 27070961 (*Preprint* <http://dx.doi.org/10.1021/acs.nanolett.6b00845>) URL <http://dx.doi.org/10.1021/acs.nanolett.6b00845>
- [84] Mochizuki M and Seki S 2015 *J. Physics: Condens. Matter* **27** 503001 URL <http://stacks.iop.org/0953-8984/27/i=50/a=503001>
- [85] Mochizuki M 2012 *Phys. Rev. Lett.* **108** 017601 URL <http://link.aps.org/doi/10.1103/PhysRevLett.108.017601>
- [86] Mochizuki M and Seki S 2013 *Phys. Rev. B* **87**(13) 134403 URL <http://link.aps.org/doi/10.1103/PhysRevB.87.134403>
- [87] Mochizuki M 2015 *Phys. Rev. Lett.* **114**(19) 197203 URL <http://link.aps.org/doi/10.1103/PhysRevLett.114.197203>
- [88] Okamura Y, Kagawa F, Seki S, Kubota M, Kawasaki M and Tokura Y 2015 *Phys. Rev. Lett.* **114**(19) 197202 URL <http://link.aps.org/doi/10.1103/PhysRevLett.114.197202>
- [89] Kataoka M 1987 *J. Phys. Soc. Jpn.* **56** 3635–3647 URL <http://dx.doi.org/10.1143/JPSJ.56.3635>
- [90] Stancil D D and Prabhakar A 2009 *Spin Waves Theory and Applications* (Springer)
- [91] Stasinopoulos I, Weichselbaumer S, Bauer A, Waizner J, Berger H, Maendl S, Garst M, Pfeiderer C and Grundler D 2017 *ArXiv e-prints (Preprint 1705.03416)*
- [92] Ishikawa Y, Noda Y, Uemura Y J, Majkrzak C F and Shirane G 1985 *Phys. Rev. B* **31** 58845893
- [93] Adams T, Chacon A, Wagner M, Bauer A, Brandl G, Pedersen B, Berger H, Lemmens P and Pfeiderer C 2012 *Phys. Rev. Lett.* **108** 237204 URL <http://link.aps.org/doi/10.1103/PhysRevLett.108.237204>
- [94] Seki S, Kim J H, Inosov D S, Georgii R, Keimer B, Ishiwata S and Tokura Y 2012 *Phys. Rev. B* **85** 220406 (R) URL <http://link.aps.org/doi/10.1103/PhysRevB.85.220406>
- [95] Janson O, Rousochatzakis I, Tsirlin A, Belesi M, Leonov A, Röler U, van den Brink J and Rosner H 2014 *Nat. Commun.* **5** 5376
- [96] Gnezdilov V P, Lamonova K V, Pashkevich Y G, Lemmens P, Berger H, Bussy F and

- Gnatchenko S L 2010 *Low Temp. Phys.* **36** 550–557 URL <http://scitation.aip.org/content/aip/journal/ltp/36/6/10.1063/1.3455808>
- [97] Miller K H, Xu X S, Berger H, Knowles E S, Arenas D J, Meisel M W and Tanner D B 2010 *Phys. Rev. B* **82**(14) 144107 URL <http://link.aps.org/doi/10.1103/PhysRevB.82.144107>
- [98] Ozerov M, Romhányi J, Belesi M, Berger H, Ansermet J P, van den Brink J, Wosnitza J, Zvyagin S A and Rousochatzakis I 2014 *Phys. Rev. Lett.* **113**(15) 157205 URL <http://link.aps.org/doi/10.1103/PhysRevLett.113.157205>
- [99] Romhányi J, van den Brink J and Rousochatzakis I 2014 *Phys. Rev. B* **90**(14) 140404 URL <http://link.aps.org/doi/10.1103/PhysRevB.90.140404>
- [100] Pocha R, Johrendt D and Pöttgen R 2000 *Chem. Mater.* **12** 2882–2887 (Preprint <http://dx.doi.org/10.1021/cm001099b>) URL <http://dx.doi.org/10.1021/cm001099b>
- [101] Kezsmarki I, Bordacs S, Milde P, Neuber E, Eng L M, White J S, Ronnow H M, Dewhurst C D, Mochizuki M, Yanai K, Nakamura H, Ehlers D, Tsurkan V and Loidl A 2015 *Nat. Mater.* **14** 1116–1122 ISSN 1476-1122 article URL <http://dx.doi.org/10.1038/nmat4402>
- [102] Tanaka M, Takayoshi H, Ishida M and Endoh Y 1985 *J. Phys. Soc. Jap.* **54** 2970–2974 (Preprint <http://dx.doi.org/10.1143/JPSJ.54.2970>) URL <http://dx.doi.org/10.1143/JPSJ.54.2970>
- [103] Ishida M, Endoh Y, Mitsuda S, Ishikawa Y and Tanaka M 1985 *J. Phys. Soc. Jap.* **54** 2975–2982 (Preprint <http://dx.doi.org/10.1143/JPSJ.54.2975>) URL <http://dx.doi.org/10.1143/JPSJ.54.2975>
- [104] Grigoriev S V, Potapova N M, Siegfried S A, Dyadkin V A, Moskvina E V, Dmitriev V, Menzel D, Dewhurst C D, Chernyshov D, Sadykov R A, Fomicheva L N and Tsvyashchenko A V 2013 *Phys. Rev. Lett.* **110** 207201
- [105] Shibata K, Z Y, Hara T, Morikawa D, Kanazawa N, Kimoto K, Ishiwata S, Matsui Y and Tokura Y 2013 *Nat. Nano.* **8** 723–728 ISSN 1748-3387 letter URL <http://dx.doi.org/10.1038/nnano.2013.174>
- [106] Bauer A, Chacon A, Wagner M, Halder M, Georgii R, Rosch A, Pfeleiderer C and Garst M 2017 *Phys. Rev. B* **95**(2) 024429 URL <https://link.aps.org/doi/10.1103/PhysRevB.95.024429>
- [107] Rohart S and Thiaville A 2013 *Phys. Rev. B* **88**(18) 184422 URL <http://link.aps.org/doi/10.1103/PhysRevB.88.184422>
- [108] Meynell S A, Wilson M N, Fritzsche H, Bogdanov A N and Monchesky T L 2014 *Phys. Rev. B* **90**(1) 014406 URL <http://link.aps.org/doi/10.1103/PhysRevB.90.014406>
- [109] Herring C and Kittel C 1951 *Phys. Rev.* **81** 869–880
- [110] Seki S, Okamura Y, Kondou K, Shibata K, Kubota M, Takagi R, Kagawa F, Kawasaki M, Tataru G, Otani Y and Tokura Y 2016 *Phys. Rev. B* **93**(23) 235131 URL <http://link.aps.org/doi/10.1103/PhysRevB.93.235131>
- [111] Sato T J, Okuyama D, Hong T, Kikkawa A, Taguchi Y, Arima T h and Tokura Y 2016 *Phys. Rev. B* **94**(14) 144420 URL <http://link.aps.org/doi/10.1103/PhysRevB.94.144420>
- [112] Grigoriev S V, Sukhanov A S, Altynbaev E V, Siegfried S A, Heinemann A, Kizhe P and Maleyev S V 2015 *Phys. Rev. B* **92** 220415
- [113] Kittel C 1948 *Phys. Rev.* **73**(2) 155–161 URL <http://link.aps.org/doi/10.1103/PhysRev.73.155>
- [114] Bauer A, Neubauer A, Franz C, Münzer W, Garst M and Pfeleiderer C 2010 *Phys. Rev. B* **82** 64404
- [115] Petrova O and Tchernyshyov O 2011 *Phys. Rev. B* **84** 214433
- [116] Janoschek M, Bernlochner F, Dunsiger S, Pfeleiderer C, Böni P, Rössli B, Link P and Rosch A 2010 *Phys. Rev. B* **81** 214436
- [117] Belitz D, Kirkpatrick T R and Rosch A 2006 *Phys. Rev. B* **73** 54431
- [118] Radzihovsky L and Lubensky T C 2011 *Phys. Rev. E* **83** 051701
- [119] Chaikin P M and Lubensky T C 1995 *Principles of Condensed Matter Physics* (Cambridge University Press)
- [120] Sievers A J and Tinkham M 1963 *Phys. Rev.* **129**(4) 1566–1571 URL <http://link.aps.org/doi/10.1103/PhysRev.129.1566>
- [121] Stasinopoulos I, Weichselbaumer S, Bauer A, Waizner J, Berger H, Garst M, Pfeleiderer C and Grundler D 2017 *ArXiv e-prints* (Preprint 1705.01582)
- [122] Bogdanov A and Hubert A 1994 *Journal of Magnetism and Magnetic Materials* **138** 255
- [123] Leonov A O, Monchesky T L, Romming N, Kubetzka A, Bogdanov A N and Wiesendanger R 2016 *New J. Phys.* **18** 065003
- [124] Mühlbauer S, Binz B, Jonietz F, Pfeleiderer C, Rosch A, Neubauer A, Georgii R and Böni P 2009 *Science (New York, NY)* **323** 915–
- [125] Buhrandt S and Fritz L 2013 *Phys. Rev. B* **88**

- [126] Waizner J 2017 *Spin wave excitations in magnetic helices and skyrmion lattices* Ph.D. thesis Universität zu Köln
- [127] Zang J, Mostovoy M, Han J H and Nagaosa N 2011 *Phys. Rev. Lett.* **107** 136804
- [128] Hasan M Z and Kane C 2010 *Rev. Mod. Phys.* **83** 3045
- [129] Roldán-Molina A, Nunez A S and Fernández-Rossier J 2016 *New J. Phys.* **18** 045015
- [130] Neusser S, Botters B and Grundler D 2008 *Phys. Rev. B* **78**(5) 054406 URL <http://link.aps.org/doi/10.1103/PhysRevB.78.054406>
- [131] Neusser S, Duerr G, Bauer H, Tacchi S, Madami M, Woltersdorf G, Gubbiotti G, Back C and Grundler D 2010 *Phys. Rev. Lett.* **105** 067208
- [132] White J S, Prša K, Huang P, Omrani A A, Živković I, Bartkowiak M, Berger H, Magrez A, Gavilano J L, Nagy G, Zang J and Rønnow H M 2014 *Phys. Rev. Lett.* **113**(10) 107203 URL <http://link.aps.org/doi/10.1103/PhysRevLett.113.107203>
- [133] Yu H, Duerr G, Huber R, Bahr M, Schwarze T, Brandl F and Grundler D 2013 *Nat. Comm.* **4** 2702
- [134] Jonietz F, Mühlbauer S, Pfleiderer C, Neubauer A, Münzer W, Bauer A, Adams T, Georgii R, Böni P, Duine R A, Everschor K, Garst M and Rosch A 2010 *Science* **330** 1648 URL <http://www.sciencemag.org/content/330/6011/1648.full.html>
- [135] Yu X Z, Kanazawa N, Zhang W Z, Nagai T, Hara T, Kimoto K, Matsui Y and Tokura Y O Y 2012 *Nat. Commun.* **3** 988 URL <http://www.nature.com/ncomms/journal/v3/n8/abs/ncomms1990.html>
- [136] Kong L and Zang J 2013 *Phys. Rev. Lett.* **111** 67203
- [137] Lin S Z, Batista C D, Reichhardt C and Saxena A 2014 *Phys. Rev. Lett.* **112**
- [138] Iwasaki J, Beekman A J and Nagaosa N 2014 *Phys. Rev. B* **89**
- [139] Schütte C and Garst M 2014 *Phys. Rev. B* **90** 094423
- [140] Zhang X, Müller J, Xia J, Garst M, Liu X and Zhou Y 2017 *ArXiv e-prints (Preprint 1701.02430)*
- [141] Mochizuki M, Yu X, Seki S, Kanazawa N, Koshibae W, Zang J, Mostovoy M, Tokura Y and Nagaosa N 2014 *Nat. Mater.* **13** 241
- [142] Pöllath S, Wild J, Heinen L, Meier T N G, Kronseder M, Tutsch L, Bauer A, Berger H, Pfleiderer C, Zweck J, Rosch A and Back C H 2017 *ArXiv e-prints (Preprint 1704.07233)*
- [143] Wang W, Beg M, Zhang B, Kuch W and Fangohr H 2015 *Phys. Rev. B* **92**(2) 020403 URL <http://link.aps.org/doi/10.1103/PhysRevB.92.020403>
- [144] Vlaminc V and Bailleul V 2008 *Science* **322** 410–413 ISSN 0036-8075 (*Preprint* <http://science.sciencemag.org/content/322/5900/410.full.pdf>) URL <http://science.sciencemag.org/content/322/5900/410>
- [145] Denisov S I and Gorobets O Y 1997 *Phys. Solid State* **39-40** 965
- [146] Garcia-Sanchez F, Borys P, Vansteenkiste A, Kim J V and Stamps R L 2014 *Phys. Rev. B* **89** 224408
- [147] Müller J, Rosch A and Garst M 2016 *New J. Phys.* **18** 065006
- [148] Zhang L, Ren J, Wang J S and Li B 2013 *Phys. Rev. B* **87**(14) 144101 URL <http://link.aps.org/doi/10.1103/PhysRevB.87.144101>
- [149] Li Zhang V, Hou C G, Di K, Siah Lim H, Ng S C, Pollard S D, Yang H and Hau Kuok M 2016 *ArXiv e-prints (Preprint 1612.06622)*
- [150] Rovillain P *et al* 2010 *Nat. Mater.* **9** 975–979
- [151] Kong L and Zang J 2013 *Phys. Rev. Lett.* **111** 067203
- [152] Lin S, Batista C, Reichhardt C and Saxena A 2014 *Phys. Rev. Lett.* **112** 187203
- [153] Kovalev A A 2014 *Phys. Rev. B* **89** 241101(R)
- [154] Zhang X, Müller J, Xia J, Garst M, Liu X and Zhou Y 2017 *ArXiv e-prints (Preprint 1701.02430)*
- [155] Lin S Z, Batista C D and Saxena A 2014 *Phys. Rev. B* **89** 024415
- [156] Kravchuk V private communication
- [157] Schroeter S and Garst M 2015 *Low Temp. Phys.* **41** 817–825
- [158] Schulz T, Ritz R, Bauer A, Halder M, Wagner M, Franz C, Pfleiderer C, Everschor K, Garst M and Rosch A 2012 *Nat. Phys.* **8** 301–304
- [159] Nagaosa N and Tokura Y 2013 *Nat. Nano.* **8** 899–911
- [160] Zhou Y, Iacocca E, Awad A A, Dumas R K, Zhang F C, Braun H B and Akerman J 2015 *Nat. Commun.* **6** 8193
- [161] Kim J V, Garcia-Sanchez F, Sampaio J a, Moreau-Luchaire C, Cros V and Fert A 2014 *Phys. Rev. B* **90**(6) 064410 URL <http://link.aps.org/doi/10.1103/PhysRevB.90.064410>
- [162] Beg M, Albert M, Bisotti M A, Cortés-Ortuño D, Wang W, Carey R, Vousden M, Hovorka O, Ciccarelli C, Spencer C S, Marrows C H and Fangohr H 2017 *Phys. Rev. B* **95** 014433

- [163] Guslienko K Y and Gareeva Z V 2017 *IEEE Magn. Lett.* **8** 4100305
- [164] Mruczkiewicz M, Krawczyk M and Guslienko K Y 2017 *Phys. Rev. B* **95**(9) 094414 URL <https://link.aps.org/doi/10.1103/PhysRevB.95.094414>
- [165] Mruczkiewicz M, Gruszecki P, Zelent M and Krawczyk M 2016 *Phys. Rev. B* **93**(17) 174429 URL <http://link.aps.org/doi/10.1103/PhysRevB.93.174429>
- [166] Ma F, Zhou Y, Braun H B and Lew W S 2015 *Nano Letters* **15** 4029–4036 pMID: 25989181 (Preprint <http://dx.doi.org/10.1021/acs.nanolett.5b00996>) URL <http://dx.doi.org/10.1021/acs.nanolett.5b00996>
- [167] Iguchi Y, Uemura S, Ueno K and Onose Y 2015 *Phys. Rev. B* **92**(18) 184419 URL <http://link.aps.org/doi/10.1103/PhysRevB.92.184419>
- [168] Garcia-Sanchez F, Borys P, Soucaille R, Adam J P, Stamps R L and Kim J V 2015 *Phys. Rev. Lett.* **114**(24) 247206 URL <http://link.aps.org/doi/10.1103/PhysRevLett.114.247206>
- [169] Borys P, Garcia-Sanchez F, Kim J V and Stamps R L 2016 *Advanced Electronic Materials* **2** 1500202
- [170] Cortes-Ortuno D and Landeros P 2013 *J. Phys.: Condens. Matter* **25** 156001 URL <http://stacks.iop.org/0953-8984/25/i=15/a=156001>
- [171] Zakeri K, Zhang Y, Prokop J, Chuang T H, Sakr N, Tang W X and Kirschner J 2010 *Phys. Rev. Lett.* **104**(13) 137203 URL <http://link.aps.org/doi/10.1103/PhysRevLett.104.137203>
- [172] Nembach H, Shaw J, Weiler M, Jué E and Silva T 2015 *Nat. Phys.* **11** 825–829
- [173] Di K, Zhang V L, Lim H S, Ng S C, Kuok M H, Qiu X and Yang H 2015 *Appl. Phys. Lett.* **106** 052403 (Preprint <http://dx.doi.org/10.1063/1.4907173>) URL <http://dx.doi.org/10.1063/1.4907173>
- [174] Lee J M, Jang C, Min B C, Lee S W, Lee K J and Chang J 2016 *Nano Letters* **16** 62–67 pMID: 26653115 (Preprint <http://dx.doi.org/10.1021/acs.nanolett.5b02732>) URL <http://dx.doi.org/10.1021/acs.nanolett.5b02732>
- [175] Ma F and Zhou Y 2014 *RSC Adv.* **4**(87) 46454–46459 URL <http://dx.doi.org/10.1039/C4RA07326F>
- [176] Costa A T, Muniz R B, Lounis S, Klautau A B and Mills D L 2010 *Phys. Rev. B* **82**(1) 014428 URL <http://link.aps.org/doi/10.1103/PhysRevB.82.014428>
- [177] Fähnle M and Illg C 2011 *J. Phys.: Condens. Matter* **23** 493201
- [178] Tserkovnyak Y, Brataas A and Bauer G E W 2002 *Phys. Rev. Lett.* **88**(11) 117601 URL <http://link.aps.org/doi/10.1103/PhysRevLett.88.117601>
- [179] Nembach H, Shaw J, Boone C and Silva T 2013 *Phys. Rev. Lett.* **110**(11) 117201 URL <http://link.aps.org/doi/10.1103/PhysRevLett.110.117201>
- [180] Demokritov S O, Hillebrands B and Slavin A N 2001 *Phys. Rep.* **348** 441–489
- [181] Zingsem B W, Farle M, Stamps R L and Camley R E 2016 *ArXiv e-prints (Preprint 1609.03417)*
- [182] Leonov A O, Togawa Y, Monchesky T L, Bogdanov A N, Kishine J, Kousaka Y, Miyagawa M, Koyama T, Akimitsu J, Koyama T, Harada K, Mori S, McGrouther D, Lamb R, Krajnak M, McVitie S, Stamps R L and Inoue K 2016 *Phys. Rev. Lett.* **117**(8) 087202 URL <http://link.aps.org/doi/10.1103/PhysRevLett.117.087202>
- [183] Du H, Che R, Kong L, Zhao X, Jin C, Wang C, Yang J, Ning W, Li R, Jin C, Chen X, Zang J, Zhang Y and Tian M 2015 *Nat. Commun.* **6** 8504 EP – article URL <http://dx.doi.org/10.1038/ncomms9504>
- [184] Damon R and Eshbach J 1961 *J. Phys. Chem. Sol.* **19** 308–320
- [185] Jorzick J, Demokritov S O, Hillebrands B, Bailleul M, Fermon C, Guslienko K Y, Slavin A N, Berkov D V and Gorn N L 2002 *Phys. Rev. Lett.* **88**(4) 047204 URL <http://link.aps.org/doi/10.1103/PhysRevLett.88.047204>
- [186] Turgut E, Park A, Nguyen K, Moehle A, Muller D A and Fuchs G D 2017 *Phys. Rev. B* **95**(13) 134416 URL <https://link.aps.org/doi/10.1103/PhysRevB.95.134416>
- [187] Togawa Y, Koyama T, Takayanagi K, Mori S, Kousaka Y, Akimitsu J, Nishihara S, Inoue K, Ovchinnikov A S and Kishine J 2012 *Phys. Rev. Lett.* **108** 107202 URL <http://link.aps.org/doi/10.1103/PhysRevLett.108.107202>
- [188] Kanazawa N, White J S, Ronnow H M, Dewhurst C D, Fujishiro Y, Tsukazaki A, Kozuka Y, Kawasaki M, Ichikawa M, Kagawa F and Tokura Y 2016 *Phys. Rev. B* **94** 184432
- [189] Kishine J and Ovchinnikov A 2009 *Phys. Rev. B* **79** 220405(R)